Pump-probe ghost imaging with SASE FELs

D. Ratner, J.P. Cryan, T.J. Lane, S. Li, and G. Stupakov

Abstract

In this paper we propose a new approach to measuring ultrafast dynamics with free-electron lasers (FELs). Ultrafast experiments are among the most promising avenues of research at x-ray FELs, with potential to reveal the chemical dynamics of charge separation, conical intersection crossing, and biologically mediated reactions. Pump-probe scanning is the standard approach to measure dynamics at x-ray FELs, but at the shortest time scales, and particularly for x-ray pump, x-ray probe experiments, the scans require challenging beam setups and can introduce systematic errors. Here we propose an alternative approach using the randomness of the self-amplified spontaneous emission (SASE) process to drive many simultaneous pump-probe experiments on each shot. Measuring the fluctuations in the incident beam's time profile on a shot-to-shot basis enables reconstruction of ultrafast dynamics down to the coherence length of the FEL without the need for pump-probe scans. Due to similarity to ghost imaging, in which spatial properties are reconstructed by measuring the incident probe's transverse properties, we call this "pump-probe ghost imaging" (PPGI). In this paper we describe the method and simulate an example experiment. We also describe an alternative implementation that uses only spectral measurements, avoiding the need for direct time-domain diagnostics, and extending the method to the attosecond regime.

One of the most valuable qualities of x-ray free-electron lasers (XFELs) is the ability to probe ultrafast dynamics down to the femtosecond (fs) scale. In the most common "pump-probe" experiments, one photon "pumps" a sample into a non-equilibrium state, and a second photon later "probes" the sample to measure the evolution of that state. Optical pump, x-ray probe measurements are now routinely used to follow chemical reactions at the femtosecond timescales intrinsic to molecular motion, an example of so-called "femto-chemistry" [1]. An important sub-class of these experiments is the x-ray pump, x-ray probe method, in which both photons are at x-ray energies. For example, a number of recent works have exploited the interaction of soft x-ray pulses with core-level electrons to probe excitations in gas phase molecular systems with atomic-site specificity [2–4]. X-ray pump, x-ray probe setups are also relevant to nano-crystallography [5]; while such experiments are ideally "damage-free" [6], careful studies have shown structural changes in proteins due to radiation-induced rearrangements may survive, highlighting the need to measure x-ray induced changes at sub-20 fs time-scales [7, 8].

Despite the success of x-ray pump-probe studies, these techniques still suffer from time-intensive machine setups, challenging systematics, and resolution that rarely exceeds 10 fs. To address these issues, here we propose a new method that exploits the chaotic nature of self-amplified spontaneous emission (SASE) XFEL pulses to extract dynamics in the fs regime. Because the SASE FEL process originates from shot-noise, each pulse consists of a random train of uncorrelated spikes (see e.g. [9]). By measuring the random substructure of individual shots in a sequence of SASE pulses, and correlating these to static sample measurements, we demonstrate that it is possible to reconstruct the time-evolution of the system at times scales as short as the SASE coherence length, typically much shorter than the duration of the FEL pulse. We emphasize that this method can be implemented with standard single-pulse operation modes, and requires no pump-probe scanning; the shot-to-shot variation is provided entirely by the randomness inherent to the SASE process.

Our proposed approach is analogous to classical ghost imaging (GI). Typical GI setups split an illumination beam into two arms, one passing through a sample to a bucket detector, and a second "reference" arm measured by a pixelated detector. Correlating fluctuations in the bucket detector to fluctuations at each pixel in the reference arm then reveals a "ghost" image of the sample. (See e.g. [10–12] for examples of x-ray GI.) In the standard application, the pixels represent transverse positions in the beam. However, by measuring fluctuations

in power rather than position, GI can also reveal temporal properties of the sample [13]. Our proposal is similar, except that we measure fluctuations in delay, the relevant quantity for pump-probe experiments. Consequently, we refer to this method as pump-probe ghost imaging (PPGI).

It is instructive to compare PPGI to the wealth of ultrafast methods employed at FELs. For example, the Linac Coherent Light Source (LCLS) has developed several two-pulse pump-probe SASE modes [14–16], and equivalent methods exist for seeded FELs as well [17, 18]. Recent advances have pushed individual pulse lengths to the sub-femtosecond regime with hard x-rays [19, 20], and the enhanced-SASE (eSASE) method can reach similar duration with soft x-rays [21]. We note each of these methods requires a potentially time-intensive setup of a special operating mode, coupled with pump-probe scanning, which can introduce systematic errors. At FLASH, an alternative method makes similar use of the chaotic nature of SASE spikes to extract dynamics at time scales shorter than the pulse length [22]. However, the FLASH technique still requires pump-probe scanning as well as a split-and-delay line to create a replica pulse, a challenge in the x-ray regime. In contrast to all of the above methods, PPGI measurements are single-pulse and passive, only requiring non-invasive measurement of the incident x-ray beam. As a result PPGI is well suited as a parasitic addition to standard FEL experiments, for example monitoring for damage in nanoxtal studies, and as a complementary method for attosecond schemes. PPGI also resembles the Hadamard transform method used at synchrotrons [23]. In the Hadamard transform, a time pattern of the synchrotron is modulated with a predetermined pattern, which is not feasible in the fs regime. By contrast, PPGI exploits the shot-to-shot variations inherent to the SASE process.

We start by considering a two-photon experiment: a pump photon induces a non-equilibrium process, and a probe photon arrives after a delay, τ, to measure some property of the sample $\boldsymbol{r}(\tau)$. For example, this modality can reveal dynamics of core-ionizied, gas-phase molecules as follows: The pump step ejects a localized core-electron resulting in a highly excited molecular cation. This highly-excited state decays via the Auger process, which results in the population of multiple dicationic states, each with equilibrium structures that differ from the initially occupied ground-state. Following the Auger process the molecular structure starts to evolve, and a second x-ray photon with energy $\hbar\omega_0$ interacts with the new time-dependent species and produces photoelectrons. Measuring the probe photoelec-

trons' kinetic energy, K_E, reveals the core-level binding energy ($E_B = \hbar\omega_0 - K_E \equiv \boldsymbol{r}(\tau)$) as a function of the inter-pulse separation (τ). This time-resolved x-ray photoelectron spectroscopy (trXPS) has been shown to provide a sensitive probe of the dynamics in excited state systems [24–26]. Similar x-ray pump-probe schemes have been used for a wide variety of science at XFELs (see e.g. [27–29]), among them measuring time-dependent change in electron density, i.e. damage, in nano-crystallography experiments [6].

Traditionally, pump-probe experiments have used two distinct "pulses," short bursts of radiation separated in time by τ. Here, we instead use a single pulse, varying in intensity over time, which is responsible for both pump and probe signals, as shown in Fig. 1a. Effectively, each pulse generates multiple, overlapping, pump-probe measurements at different delays. In the simplest implementation, we make the following additional assumptions:

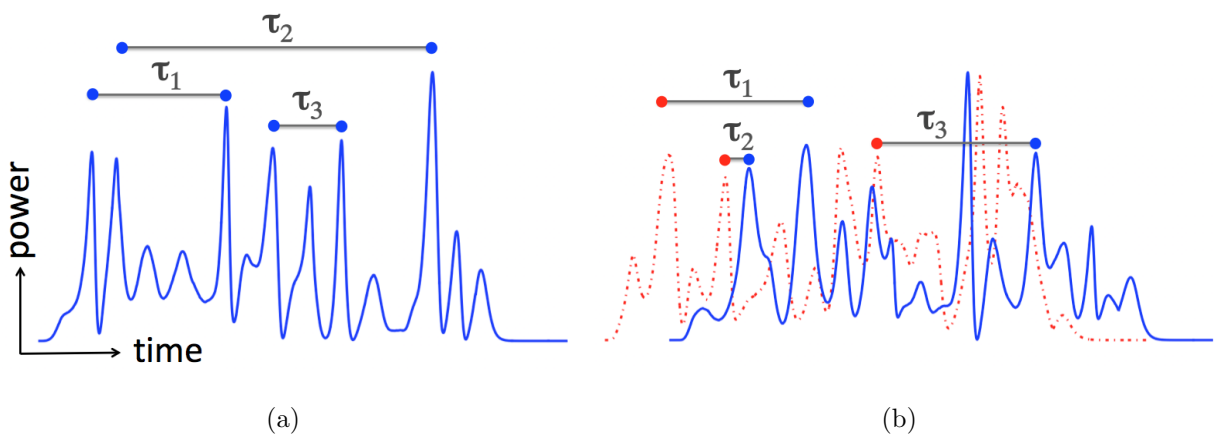

FIG. 1. a) The simplest realization with a single SASE pulse: photons separated by different delays (e.g. τ_1, τ_2, τ_3) effectively drive independent pump-probe experiments within the same pulse. b) More complicated setups are also possible, for example pumping with one wavelength (red dashed line) and probing with another (blue solid line). In both cases, the temporal resolution of the reconstruction is determined by the spike width or measurement resolution, not the pulse duration as in a traditional pump-probe setup.

1. The probability of a pump photon inducing an excitation is proportional to the instantaneous power.

2. The probability of a probe photon generating a measurable signal is proportional to the instantaneous power.

These conditions hold broadly for many XFEL experiments. We note that 'excitation' does not necessarily refer to electronic states, but could include, for example, a damage event to a protein. While these assumptions allow a simple formulation of the problem, PPGI can be applied even if one or both are violated.

We can then write the ensemble distribution of states $\boldsymbol{s}(t)$ at a time t in the "i-th" pulse as

$$\boldsymbol{s}_i(t) = \int_{-\infty}^{t} \boldsymbol{p}_i(t')\, \boldsymbol{r}(t-t')\, dt' \,. \tag{1}$$

Here, t' is the time at which an individual member in the population was excited, and $\boldsymbol{p}_i(t)$ is the power profile of the pulse. In atomic and molecular systems, $\boldsymbol{r}(\tau)$ evolves over short time scales, and we can only measure a time-averaged version of $\boldsymbol{s}_i(t)$, which we will call m_i. With the second assumption that the measured signal m_i is proportional to the x-ray power, we find

$$m_i = \int_{-\infty}^{\infty} \boldsymbol{p}_i(t)\, \boldsymbol{s}_i(t)\, dt = \int_{0}^{\infty} \boldsymbol{a}_i(\tau)\, \boldsymbol{r}(\tau) d\tau \,, \tag{2}$$

where we have used shorthand for the autocorrelation, $\boldsymbol{a}_i(\tau) \equiv \int_{-\infty}^{\infty} \boldsymbol{p}_i(t)\, \boldsymbol{p}_i(t-\tau)\, dt$. Our goal is to recover $\boldsymbol{r}(\tau)$ from the measurements m_i and $\boldsymbol{a}_i(\tau)$.

In a practical implementation with N_m pulses and N_τ discretized delays, the autocorrelations form a matrix $\boldsymbol{A} \in \mathbb{R}^{N_m \times N_\tau}$. Likewise, the individual measurements m_i comprise a column vector $\boldsymbol{m} \in \mathbb{R}^{N_m}$. Then we may write

$$\boldsymbol{m} = \boldsymbol{A}\boldsymbol{r} \,, \tag{3}$$

where $\boldsymbol{r} \in \mathbb{R}^{N_\tau}$ is the discretized version of $\boldsymbol{r}(\tau)$. So long as we obtain sufficient pulses of different power profiles, we may *infer* the underlying system dynamics $\boldsymbol{r}$ by solving this set of linear equations. The experimental schematic is shown in Fig. 2.

The derivation of Eq. 2 implicitly assumes that pump and probe events are independent, which is satisfied if the pump signal does not contribute to m_i. For example, in the cation experiment described earlier, photoelectrons from the initial pump event are separated by many eV in energy from those from the probe cation, and the former can be excluded from the bucket detector. However, even when this assumption is violated, PPGI can still be applied; because the pump signal is proportional to the pulse energy rather than the autocorrelation, the pump events will only contribute an uncorrelated noise term to Eq. 3. The presence of additional background increases the number of examples needed for

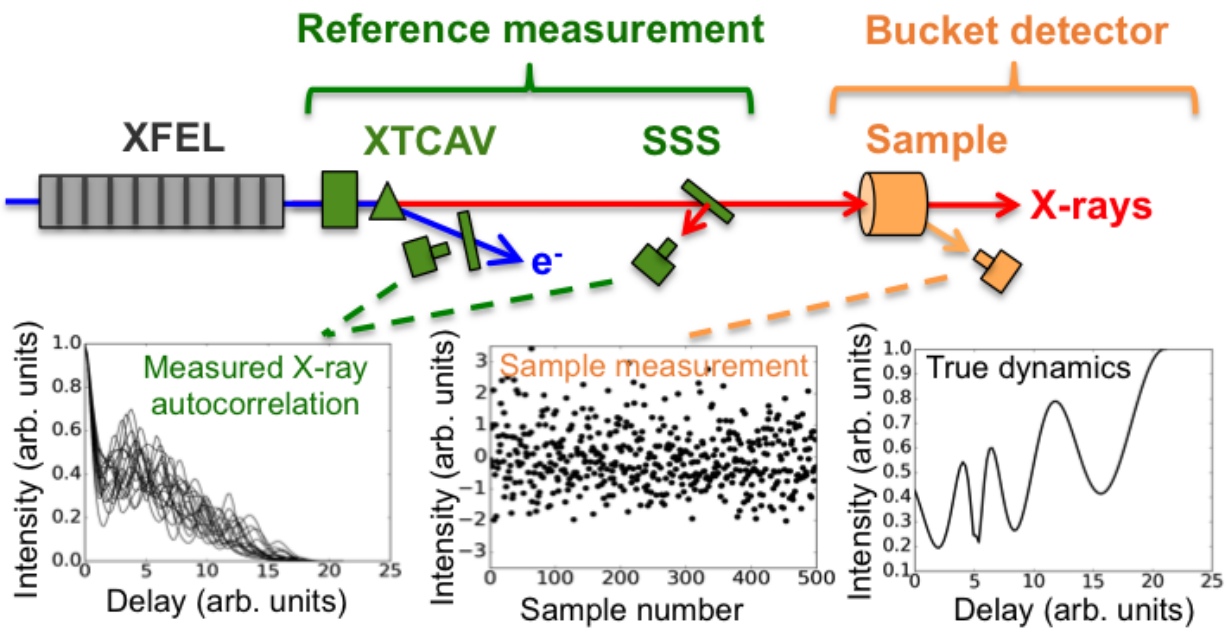

FIG. 2. Schematic of general PPGI scheme. Time (e.g. XTCAV) or frequency domain (e.g. single-shot spectrometer, SSS) measurements record the auto-correlation on a shot-by-shot basis upstream of the sample (lower left). In the terminology of ghost imaging, these reference measurements record the fluctuations incident on the sample. "Bucket" measurements downstream of the sample, e.g. photoelectron counts, contain no explicit time information (lower middle). Correlating shot-to-shot variations in sample measurements with the corresponding measured SASE fluctuations reveals the true sample dynamics (lower right).

convergence, but it does not affect the identifiability of Eq. 3. The same argument applies to avoiding signal from multiple excitations.

In the traditional ghost imaging formalism, $\boldsymbol{r}$ is found by explicitly calculating the correlation between $\boldsymbol{m}$ and $\boldsymbol{A}$. An alternative compressed sensing formalism finds the most likely solution $\boldsymbol{r}^*$ by optimizing a cost function [30, 31], enabling the addition of arbitrary priors to constrain the solution. For example, using L-2 regularized least-squares regression (i.e. Tikhonov or ridge regression), we solve for an optimal solution $\boldsymbol{r}^*$ from

$$\boldsymbol{r}^* = \text{argmin}_{\boldsymbol{r}} \left(||\boldsymbol{m} - \boldsymbol{A}\boldsymbol{r}||^2 + \lambda ||\boldsymbol{r}||^2 \right) , \tag{4}$$

with regularization parameter λ. Additional physically-inspired constraints e.g. non-negativity, $\boldsymbol{r}^* \geq 0$, or causality, $\boldsymbol{r}(\tau < 0) = 0$, can further improve the solution or reduce the required number of measurements, N_m. Compressed sensing has been found to increase the

convergence rate for ghost imaging, even allowing reconstruction with fewer samples than pixels (see e.g. [32–36]).

For a typical ghost imaging setup, a beam-splitter upstream of the sample sends a portion of the x-ray beam to a reference arm to measure the incident radiation pattern. Due to the challenge of measuring the shot-to-shot power of an XFEL beam, it is easier to infer $\boldsymbol{p}_i(t)$ from the spent electron beam, e.g. with an x-band transverse cavity (XTCAV) [37] or with an optical afterburner [38]. In this scenario, the electron beam plays the role of the reference arm (Fig. 2). It may also be possible to directly measure the x-ray beam, for example by angular streaking [39].

To this point, we have assumed it is possible to directly measure the power, $\boldsymbol{p}(t)$, e.g. using an XTCAV. If temporal resolution of the power measurement limits the reconstruction resolution, combining partial time-domain information with spectral measurements enables refinement of $\boldsymbol{p}(t)$ using phase retrieval algorithms [40]. Alternatively, we may notice that Eq. 3 requires only the second-order autocorrelation, and there is no need to explicitly measure the power. By the Wiener-Khinchin theorem, the first-order autocorrelation can be calculated directly from the spectral power. For arbitrary fields there is not a well-determined relation between $\boldsymbol{A}$ and $\boldsymbol{A}^{(f)}$, but for the special case of a SASE FEL, the two quantities are highly correlated. In the SI we derive an analytical expression for this correlation in the case of Gaussian wave packets, a common model for an FEL [9]. Fig. 3 shows the relation also holds in 1-D FEL simulations. Therefore if we simply treat $\boldsymbol{A}^{(f)}$ as a noisy version of $\boldsymbol{A}$ in Eq. 3, we still expect to recover features of $\boldsymbol{r}$.

Spectral power measurements have several advantages. In general, spectral measurements at XFELs are simpler than those in the time domain; for example, at LCLS the thin crystal hard x-ray single-shot spectrometer (SSS) [41] provides high resolution spectra on a shot-by-shot basis simultaneously with sample measurements. Spectrometers can also operate at higher repetition rate compared to the XTCAV, which runs only at 120 Hz. Finally, the autocorrelation resolution for the spectral approach is limited only by the fluctuations in $\boldsymbol{a}_i$, determined by the SASE coherence length, t_{coh}. As an example, a hard x-ray FEL such as the Linac Coherent Light-Source (LCLS) [42] lasing at 1.5 Å has $t_{\text{coh}} \sim 300$ attoseconds, giving sub-femtosecond resolution without the need for generating ultra-short pulses, pump-probe scanning, or even relative timing of two pulses.

To illustrate the PPGI method, we simulate an experiment with $\boldsymbol{r}$ given by a line-out from

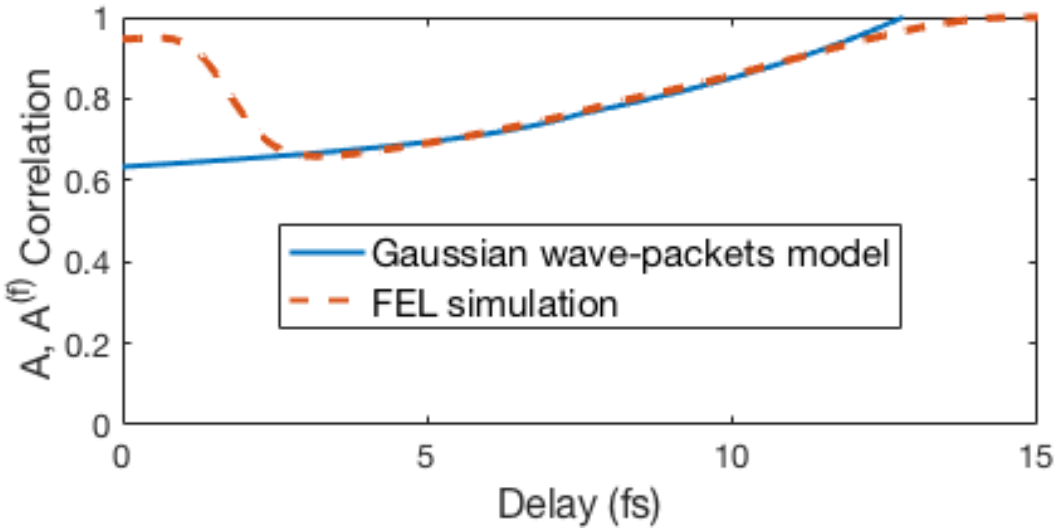

FIG. 3. Fluctuations in $\boldsymbol{A}^{(f)}$ and $\boldsymbol{A}$ are strongly correlated for delays $t_{\text{coh}} \ll \tau < T$, with pulse length T and coherence length t_{coh}. Figure shows the Pearson correlation between $\boldsymbol{A}^{(f)}$ and $\boldsymbol{A}$ for both an analytical model of Gaussian wave-packets (solid blue line, see SI) and 1D simulations of a pre-saturation FEL with parameters of Table I (dashed red line).

the "Eggholder" function, a standard artificial landscape test function. We simulate the x-ray pulses using a 1D FEL code [43] with parameters typical for LCLS soft x-ray operation, and running without taper about 3 gainlengths past saturation, which we find empirically results in the best reconstructions (see SI Sec. 1). From the power we calculate the true autocorrelations, $\boldsymbol{A}^*$, and true signal, $\boldsymbol{m}^* = \boldsymbol{A}^* \times \boldsymbol{r}$. To account for noise and instrument resolution, Δ_t, we apply Gaussian noise and blurring to $\boldsymbol{A}^*$ to produce measurements $\boldsymbol{A}$, and add Gaussian noise to $\boldsymbol{m}^*$ to produce measurements $\boldsymbol{m}$. The reconstruction then uses ridge (Eq. 4) with an additional non-negativity constraint. Table I summarizes the simulated parameters and Fig. 4 shows the resulting reconstruction. The reconstruction converges to the ground truth in the range $t_{\text{coh}} \lesssim \tau \lesssim T$, with the resolution limited by the larger of the SASE coherence length t_{coh} and the instrument resolution. For $\tau \lesssim t_{\text{coh}}$ and $\tau \gtrsim T$ each measurement $\boldsymbol{a}_i$ is nearly identical, making $\boldsymbol{A}$ poorly conditioned, and we do not expect to recover $\boldsymbol{r}$ in this range.

We also treat the same problem using the spectral approach. In this case, starting from the simulated spectral power, we add Gaussian noise and blurring from the instrumental resolution, Δ_ν, and then calculate the Fourier transform, $\boldsymbol{A}^{(f)}$. We shift and scale $\boldsymbol{A}^{(f)}$ so

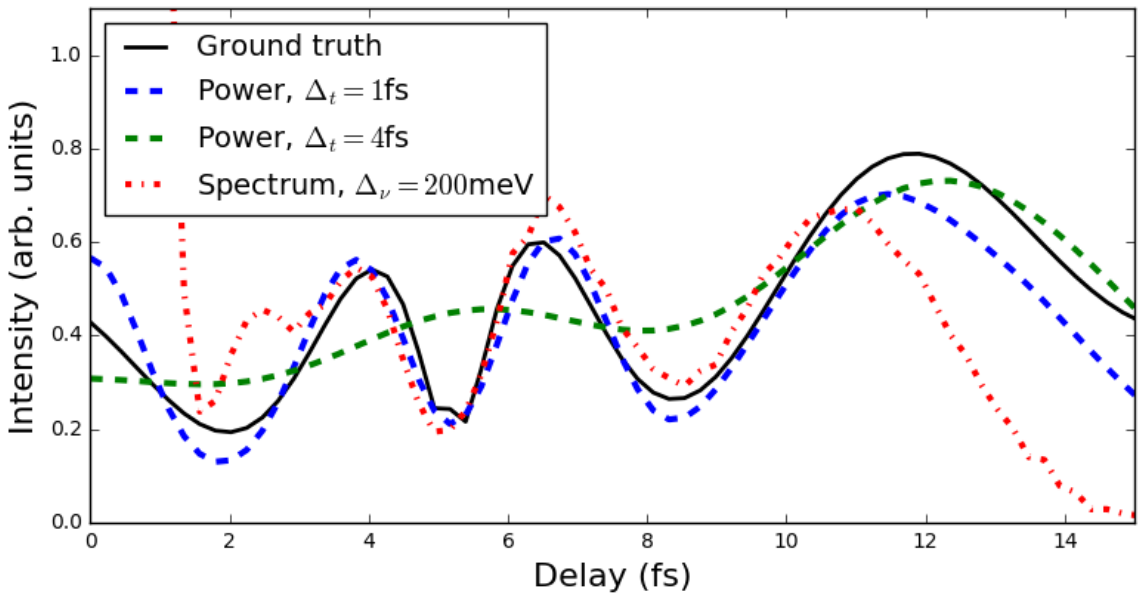

FIG. 4. Illustration of PPGI using simulation parameters from Table I and measurements of either power (time domain) or spectrum (frequency domain). Ground truth taken from the Eggholder artificial landscape function.

that both the mean and mean fluctuation amplitudes match those of $\boldsymbol{A}$, and use the result in place of $\boldsymbol{A}$ in Eq. 4. We then scale the overall amplitude of $\boldsymbol{r}^*$ to minimize mean squared error (MSE). Because of the correlation between $\boldsymbol{A}^{(f)}$ and $\boldsymbol{A}$ for FEL radiation, it is still possible to recover a good approximation of $\boldsymbol{r}$ (Fig. 4). Whereas in the time domain case instrumental resolution limits the reconstruction of sharp features, in the spectral version the spectrometer resolution cuts off reconstruction at long delays, but preserves sharp features in the range $2t_c \lesssim \tau \lesssim 3\hbar/\Delta_\nu$.

To this point, we have assumed each sample measurement is a single scalar. However, XFEL experiments commonly measure a vector of parameters, $\boldsymbol{m}_i(y)$, with multiple buckets, N_y. Here the y dimension represents a measured experimental parameter, for example an electron or x-ray spectrum emitted by the sample. In this case, $\boldsymbol{m} \to \boldsymbol{M} \in \mathbb{R}^{N_M \times N_y}$ and

X-ray photon energy (eV)	500
X-ray FWHM pulse length, T (fs)	15
X-ray coherence length, t_{coh} (fs)	1.6
XTCAV FWHM resolution, Δ_t (fs)	1 or 4
SSS FWHM resolution, Δ_ν (meV)	200
Signal to noise ratio (FWHM)	10
Number of shots, N_m	100k

TABLE I. Parameters for simulations based on LCLS soft x-ray operation. Signal-to-noise is relative to half-max of signal, and is added to $\boldsymbol{M}$, $\boldsymbol{A}$, and $\boldsymbol{A}^{(f)}$.

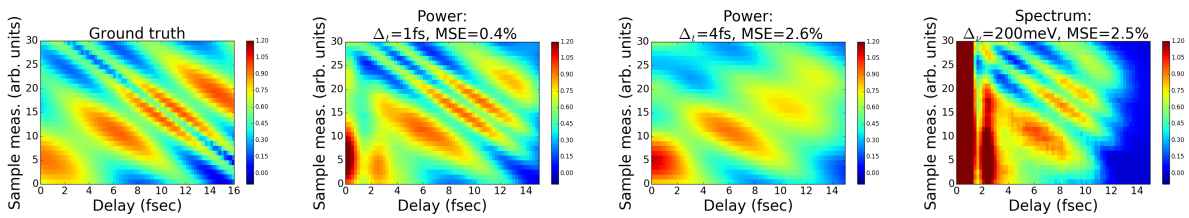

(a) (b) (c) (d)

FIG. 5. Left, an example taken from the Eggholder artificial landscape function to represent $\boldsymbol{r}$. The x-axis corresponds to pump-probe delay, and the y-axis represents a sample measurement, for example intensity of a measured x-ray or electron spectrum emitted by the sample. Reconstructions assume LCLS soft x-ray parameters (Table I) and instrumental FWHM resolution of $\Delta_t = 1$ fs (b) and $\Delta_t = 4$ fs (c) for power measurements, and $\Delta_\nu = 200$ meV for spectral measurements (d). MSE calculated over the range 4 to 11 fs.

$\boldsymbol{r} \to \boldsymbol{R} \in \mathbb{R}^{N_\tau \times N_y}$. In all other aspects the problem is identical, and $\boldsymbol{R}$ is still found by solving Eq. 4. To demonstrate, Fig. 5 shows a simulation result with $\boldsymbol{R}$ a 2-D excerpt from the Eggholder landscape function.

For simplicity, we have used a simple least squares solution. Though sufficient for the example of Fig. 5, more sophisticated approaches may further improve results. For example, we have significant errors on the independent variable, $\boldsymbol{A} \neq \boldsymbol{A}^*$, creating what is commonly known as an "errors-in-variables" problem. Least squares solutions are sub-optimal, e.g. due to regression dilution, compared to results from methods such as total least squares.

Secondly, we have retrieved each row of $\boldsymbol{R}$ independently. Modern image analysis tools, for example the alternating direction method of multipliers (ADMM) [44], enable simultaneous reconstruction of the entire process, $\boldsymbol{R}$. This permits the inclusion of additional priors, such as smoothness in both time and energy, that can further improve estimates of $\boldsymbol{R}$.

In this paper, we have introduced a new approach to extracting dynamics from XFEL pump-probe experiments. While specialized techniques such as eSASE and nonlinear compression have shown great promise to reach the attosecond regime, these methods require complex setups [19] and dedicated hardware [20, 21], and involve pump-probe scans that introduce systematic error and require precision timing measurements that limit the time resolution. Moreover, the shortest sub-femtosecond operating modes [19] are not easily incorporated into pump-probe schemes. By contrast, the ghost imaging technique presented here needs only a single x-ray pulse, can be performed at any XFEL without modification, can reach sub-femtosecond resolution, is equally applicable to hard and soft x-rays, and does not require any special beam tuning. As a passive scheme that does not rely on time scans, PPGI is well suited as a parasitic measurement, e.g. for monitoring nano-crystallography damage [6, 8]. With sufficient data, PPGI can recover the short-delay (and thus damage-free) Bragg intensities. Spectral PPGI, though noisier and limited to linear systems, may be the easiest to test experimentally as it requires only a spectrometer. It also may be possible to improve the temporal resolution by reducing the FEL coherence length, e.g. using eSASE [21] or the microbunching instability [45, 46].

While we have focused on the simplest case of a single pulse, the method is easily generalized to more complex setups including two-color x-ray schemes (e.g. [14, 15]) or even optical-pump, x-ray probe [47] with the addition of a timing system [48] (Fig. 1b). Finally, while we have assumed each sample has been pumped a single time, we can also relax that assumption and allow for multiple interactions between the target and incident x-ray field (complementing e.g. four-wave mixing protocols [49]). Given that multi-photon excitations are inherently rare events, such schemes will benefit greatly from the increased brightness of the superconducting XFEL facilities currently under development.

We would like to thank Zhirong Huang, Tim Maxwell, and Gordon Wetzstein for their help. This work was supported by U.S. Department of Energy Office of Science under Contract No. DE-AC02-76SF00515. JPC contribution is supported by U.S. Department of Energy (DOE), Office of Science, Basic Energy Sciences (BES), Chemical Sciences, Geo-

sciences, and Biosciences Division.

[1] A. Zewail, "Femtochemistry: Atomic-scale dynamics of the chemical bond," J. Phys. Chem. A **104**, 24 (2000).

[2] T. J. A. Wolf, R. H. Myhre, J. P. Cryan, S. Coriani, R. J. Squibb, A. Battistoni, N. Berrah, C. Bostedt, P. Bucksbaum, G. Coslovich, R. Feifel, K. J. Gaffney, J. Grilj, T. J. Martinez, S. Miyabe, S. P. Moeller, M. Mucke, A. Natan, R. Obaid, T. Osipov, O. Plekan, S. Wang, H. Koch, and M. Guhr, "Probing ultrafast $\pi\pi*/n\pi*$ internal conversion in organic chromophores via k-edge resonant absorption," Nature Communications **8**, 29 (2017).

[3] Andrew R. Attar, Aditi Bhattacherjee, C. D. Pemmaraju, Kirsten Schnorr, Kristina D. Closser, David Prendergast, and Stephen R. Leone, "Femtosecond x-ray spectroscopy of an electrocyclic ring-opening reaction," Science **356**, 6333 (2017).

[4] Yoann Pertot, Cedric Schmidt, Mary Matthews, Adrien Chauvet, Martin Huppert, Vit Svoboda, Aaron von Conta, Andres Tehlar, Denitsa Baykusheva, Jean-Pierre Wolf, and Hans Jakob Worner, "Time-resolved x-ray absorption spectroscopy with a water window high-harmonic source," Science **355**, 6322 (2017).

[5] Henry N. Chapman, Petra Fromme, Anton Barty, Thomas A. White, Richard A. Kirian, Andrew Aquila, Mark S. Hunter, Joachim Schulz, Daniel P. DePonte, Uwe Weierstall, R. Bruce Doak, Filipe R. N. C. Maia, Andrew V. Martin, Ilme Schlichting, Lukas Lomb, Nicola Coppola, Robert L. Shoeman, Sascha W. Epp, Robert Hartmann, Daniel Rolles, Artem Rudenko, Lutz Foucar, Nils Kimmel, Georg Weidenspointner, Peter Holl, Mengning Liang, Miriam Barthelmess, Carl Caleman, Sebastien Boutet, Michael J. Bogan, Jacek Krzywinski, Christoph Bostedt, Sasa Bajt, Lars Gumprecht, Benedikt Rudek, Benjamin Erk, Carlo Schmidt, Andre Homke, Christian Reich, Daniel Pietschner, Lothar Struder, Gunter Hauser, Hubert Gorke, Joachim Ullrich, Sven Herrmann, Gerhard Schaller, Florian Schopper, Heike Soltau, Kai-Uwe Kuhnel, Marc Messerschmidt, John D. Bozek, Stefan P. Hau-Riege, Matthias Frank, Christina Y. Hampton, Raymond G. Sierra, Dmitri Starodub, Garth J. Williams, Janos Hajdu, Nicusor Timneanu, M. Marvin Seibert, Jakob Andreasson, Andrea Rocker, Olof Jonsson, Martin Svenda, Stephan Stern, Karol Nass, Robert Andritschke, Claus-Dieter Schroter, Faton Krasniqi, Mario Bott, Kevin E. Schmidt, Xiaoyu Wang, Ingo Grotjohann, James M. Holton,

Thomas R. M. Barends, Richard Neutze, Stefano Marchesini, Raimund Fromme, Sebastian Schorb, Daniela Rupp, Marcus Adolph, Tais Gorkhover, Inger Andersson, Helmut Hirsemann, Guillaume Potdevin, Heinz Graafsma, Bjorn Nilsson, and John C. H. Spence, "Femtosecond x-ray protein nanocrystallography," Nature **470**, 73–77 (2011).

[6] Anton Barty, Carl Caleman, Andrew Aquila, Nicusor Timneanu, Lukas Lomb, Thomas A. White, Jakob Andreasson, David Arnlund, Sasa Bajt, Thomas R. M. Barends, Miriam Barthelmess, Michael J. Bogan, Christoph Bostedt, John D. Bozek, Ryan Coffee, Nicola Coppola, Jan Davidsson, Daniel P. DePonte, R. Bruce Doak, Tomas Ekeberg, Veit Elser, Sascha W. Epp, Benjamin Erk, Holger Fleckenstein, Lutz Foucar, Petra Fromme, Heinz Graafsma, Lars Gumprecht, Janos Hajdu, Christina Y. Hampton, Robert Hartmann, Andreas Hartmann, Gunter Hauser, Helmut Hirsemann, Peter Holl, Mark S. Hunter, Linda Johansson, Stephan Kassemeyer, Nils Kimmel, Richard A. Kirian, Mengning Liang, Filipe R. N. C. Maia, Erik Malmerberg, Stefano Marchesini, Andrew V. Martin, Karol Nass, Richard Neutze, Christian Reich, Daniel Rolles, Benedikt Rudek, Artem Rudenko, Howard Scott, Ilme Schlichting, Joachim Schulz, M. Marvin Seibert, Robert L. Shoeman, Raymond G. Sierra, Heike Soltau, John C. H. Spence, Francesco Stellato, Stephan Stern, Lothar Struder, Joachim Ullrich, X. Wang, Georg Weidenspointner, Uwe Weierstall, Cornelia B. Wunderer, and Henry N. Chapman, "Self-terminating diffraction gates femtosecond x-ray nanocrystallography measurements," Nature Photonics **6**, 35–40 (2012).

[7] L. Galli, S.-K. Son, M. Klinge, S. Bajt, A. Barty, R. Bean, C. Betzel, K. R. Beyerlein, C. Caleman, R. B. Doak, M. Duszenko, H. Fleckenstein, C. Gati, B. Hunt, R. A. Kirian, M. Liang, M. H. Nanao, K. Nass, D. Oberthr, L. Redecke, R. Shoeman, F. Stellato, C. H. Yoon, T. A. White, O. Yefanov, J. Spence, and H. N. Chapman, "Electronic damage in s atoms in a native protein crystal induced by an intense x-ray free-electron laser pulse," Structural Dynamics **2**, 041703 (2015).

[8] K. Nass, L. Foucar, T. R. M. Barends, E. Hartmann, S. Botha, R. L. Shoeman, R. B. Doak, R. Alonso-Mori, A. Aquila, S. Bajt, A. Barty, R. Bean, K. R. Beyerlein, M. Bublitz, N. Drachmann, J. Gregersen, H. O. Jonsson, W. Kabsch, S. Kassemeyer, J. E. Koglin, M. Krumrey, D. Mattle, M. Messerschmidt, P. Nissen, L. Reinhard, O. Sitsel, D. Sokaras, G. J. Williams, S. Hau-Riege, N. Timneanu, C. Caleman, H. N. Chapman, S. Boutet, and I. Schlichting, "Indications of radiation damage in ferredoxin microcrystals using high-intensity x-fel beams," J.

Synchrotron Rad. **22**, 225 (2015).

[9] Kwang-Je Kim, Zhirong Huang, and Ryan Lindberg, *Synchrotron radiation and free-electron lasers* (Cambridge University Press, 2017).

[10] D. Pelliccia, A. Rack, M. Scheel, V. Cantelli, and D. M. Paganin, "Experimental x-ray ghost imaging," Phys. Rev. Lett. **117**, 113902 (2016).

[11] Hong Yu, Ronghua Lu, Shensheng Han, Honglan Xie, Guohao Du, Tiqiao Xiao, and Daming Zhu, "Fourier-transform ghost imaging with hard x rays," Phys. Rev. Lett. **117**, 113901 (2016).

[12] Andrew. M. Kingston, Daniele Pelliccia, Alexander Rack, Margie P. Olbinado, Yin Cheng, Glenn R. Myers, and David M. Paganin, "Ghost tomography," Optica **5**, 1516–1520 (2018).

[13] Piotr Ryczkowski, Margaux Barbier, Ari T. Friberg, John M. Dudley, and Goery Genty, "Ghost imaging in the time domain," Nature Photonics **10**, 167 (2016).

[14] A. A. Lutman, R. Coffee, Y. Ding, Z. Huang, J. Krzywinski, T. Maxwell, M. Messerschmidt, and H.-D. Nuhn, "Experimental demonstration of femtosecond two-color x-ray free-electron lasers," Phys. Rev. Lett. **110**, 134801 (2013).

[15] A. Marinelli, D. Ratner, A. A. Lutman, J. Turner, J. Welch, F.-J. Decker, H. Loos, C. Behrens, S. Gilevich, A. A. Miahnahri, S. Vetter, T.J. Maxwell, Y. Ding, R. Coffee, S. Wakatsuki, and Z. Huang, "High intensity double pulse x-ray free-electron laser," Nature Comm. **6**, 6369 (2015).

[16] Alberto A. Lutman, Timothy J. Maxwell, James P. MacArthur, Marc W. Guetg, Nora Berrah, Ryan N. Coffee, Yuantao Ding, Zhirong Huang, Agostino Marinelli, Stefan Moeller, and Johann C. U. Zemella, "Fresh-slice multicolour x-ray free-electron lasers," Nature Photonics **10**, 745 (2016).

[17] E. Allaria, D. Castronovo, P. Cinquegrana, P. Craievich, M. Dal Forno, M. B. Danailov, G. D'Auria, A. Demidovich, G. De Ninno, S. Di Mitri, B. Diviacco, W. M. Fawley, M. Ferianis, E. Ferrari, L. Froehlich, G. Gaio, D. Gauthier, L. Giannessi, R. Ivanov, B. Mahieu, N. Mahne, I. Nikolov, F. Parmigiani, G. Penco, L. Raimondi, C. Scafuri, C. Serpico, P. Sigalotti, S. Spampinati, C. Spezzani, M. Svandrlik, C. Svetina, M. Trovo, M. Veronese, D. Zangrando, and M. Zangrando, "Two-stage seeded soft-x-ray free-electron laser," Nature Photonics **7**, 913 (2013).

[18] David Gauthier, Primo Rebernik Ribic, Giovanni DeNinno, Enrico Allaria, Paolo Cinquegrana, Miltcho Bojanov Danailov, Alexander Demidovich, Eugenio Ferrari, and Luca Gian-

nessi, "Generation of phase-locked pulses from a seeded free-electron laser," Phys. Rev. Lett. **116**, 024801 (2016).

[19] S. Huang, Y. Ding, Y. Feng, E. Hemsing, Z. Huang, J. Krzywinski, A. A. Lutman, A. Marinelli, T. J. Maxwell, and D. Zhu, "Generating single-spike hard x-ray pulses with nonlinear bunch compression in free-electron lasers," Phys. Rev. Lett. **119**, 154801 (2017).

[20] A. Marinelli, J. MacArthur, P. Emma, M. Guetg, C. Field, D. Kharakh, A. A. Lutman, Y. Ding, and Z. Huang, "Experimental demonstration of a single-spike hard-x-ray free-electron laser starting from noise," Appl. Phys. Lett. **111**, 151101 (2017).

[21] A. A. Zholents and W. M. Fawley, "Proposal for intense attosecond radiation from an x-ray free-electron laser," Phys. Rev. Lett. **92**, 224801 (2004).

[22] Kristina Meyer, Christian Ott, Philipp Raith, Andreas Kaldun, Yuhai Jiang, Arne Senftleben, Moritz Kurka, Robert Moshammer, Joachim Ullrich, and Thomas Pfeifer, "Noisy optical pulses enhance the temporal resolution of pump-probe spectroscopy," Phys. Rev. Lett **108**, 098302 (2012).

[23] Briony A Yorke, Godfrey S Beddard, Robin L Owen, and Arwen R Pearson, "Time-resolved crystallography using the hadamard transform," Nature Methods **11**, 1131 (2014).

[24] S Hellmann, C Sohrt, M Beye, T Rohwer, F Sorgenfrei, M Marczynski-Buhlow, M Kallane, H Redlin, F Hennies, M Bauer, A Fohlisch, L Kipp, W Wurth, and K Rossnagel, "Time-resolved x-ray photoelectron spectroscopy at FLASH," New Journal of Physics **14**, 013062 (2012).

[25] Andrey Shavorskiy, Amy Cordones, Josh Vura-Weis, Katrin Siefermann, Daniel Slaughter, Felix Sturm, Fabian Weise, Hendrik Bluhm, Matthew Strader, Hana Cho, Ming-Fu Lin, Camila Bacellar, Champak Khurmi, Marcus Hertlein, Jinghua Guo, Tolek Tyliszczak, David Prendergast, Giacomo Coslovich, Joseph Robinson, Robert A Kaindl, Robert W Schoenlein, Ali Belkacem, Thorsten Weber, Daniel M Neumark, Stephen R Leone, Dennis Nordlund, Hirohito Ogasawara, Anders R Nilsson, Oleg Krupin, Joshua J Turner, William F Schlotter, Michael R Holmes, Philip A Heimann, Marc Messerschmidt, Michael P Minitti, Martin Beye, Sheraz Gul, Jin Z Zhang, Nils Huse, and Oliver Gessner, "Time-resolved x-ray photoelectron spectroscopy techniques for real-time studies of interfacial charge transfer dynamics," AIP Conference Proceedings **1525**, 475 (2013).

[26] Chelsea E. Liekhus-Schmaltz, Ian Tenney, Timur Osipov, Alvaro Sanchez-Gonzalez, Nora

Berrah, Rebecca Boll, Cedric Bomme, Christoph Bostedt, John D. Bozek, Sebastian Carron, Ryan Coffee, Julien Devin, Benjamin Erk, Ken R. Ferguson, Robert W. Field, Lutz Foucar, Leszek J. Frasinski, James M. Glownia, Markus Guhr, Andrei Kamalov, Jacek Krzywinski, Heng Li, Jonathan P. Marangos, Todd J. Martinez, Brian K. McFarland, Shungo Miyabe, Brendan Murphy, Adi Natan, Daniel Rolles, Artem Rudenko, Marco Siano, Emma R. Simpson, Limor Spector, Michele Swiggers, Daniel Walke, Song Wang, Thorsten Weber, Philip H. Bucksbaum, and Vladimir S. Petrovic, "Ultrafast isomerization initiated by x-ray core ionization," Nature Comm. **6**, 8199 (2015).

[27] Ken R. Ferguson, Maximilian Bucher, Tais Gorkhover, Sébastien Boutet, Hironobu Fukuzawa, Jason E. Koglin, Yoshiaki Kumagai, Alberto Lutman, Agostino Marinelli, Marc Messerschmidt, Kiyonobu Nagaya, Jim Turner, Kiyoshi Ueda, Garth J. Williams, Philip H. Bucksbaum, and Christoph Bostedt, "Transient lattice contraction in the solid-to-plasma transition," Science Advances **2** (2016).

[28] Ichiro Inoue, Yuichi Inubushi, Takahiro Sato, Kensuke Tono, Tetsuo Katayama, Takashi Kameshima, Kanade Ogawa, Tadashi Togashi, Shigeki Owada, Yoshiyuki Amemiya, Takashi Tanaka, Toru Hara, and Makina Yabashi, "Observation of femtosecond x-ray interactions with matter using an x-ray–x-ray pump–probe scheme," Proceedings of the National Academy of Sciences **113**, 1492–1497 (2016).

[29] Claudiu A. Stan, Despina Milathianaki, Hartawan Laksmono, Raymond G. Sierra, Trevor A. McQueen, Marc Messerschmidt, Garth J. Williams, Jason E. Koglin, Thomas J. Lane, Matt J. Hayes, Serge A. H. Guillet, Mengning Liang, Andrew L. Aquila, Philip R. Willmott, Joseph S. Robinson, Karl L. Gumerlock, Sabine Botha, Karol Nass, Ilme Schlichting, Robert L. Shoeman, Howard A. Stone, and Sebastien Boutet, "Liquid explosions induced by x-ray laser pulses," Nature Physics **12**, 966 (2016).

[30] E. J. Candes, J. Romberg, and T. Tao, "Robust uncertainty principles: exact signal reconstruction from highly incomplete frequency information," IEEE Trans. Inf. Theory **52**, 489 (2006).

[31] Ori Katz, Yaron Bromberg, and Yaron Silberberg, "Recoil-induced subradiance in an ultracold atomic gas," Appl. Phys. Lett. **95**, 131110 (2009).

[32] Liu Jiying, Zhu Jubo, Lu Chuan, and Huang Shisheng, "High-quality quantum-imaging algorithm and experiment based on compressive sensing," Opt. Lett. **35**, 1206–1208 (2010).

[33] Petros Zerom, Kam Wai Clifford Chan, John C. Howell, and Robert W. Boyd, "Entangled-photon compressive ghost imaging," Phys. Rev. A **84**, 061804 (2011).

[34] Vladimir Katkovnik and Jaakko Astola, "Compressive sensing computational ghost imaging," J. Opt. Soc. Am. A **29**, 1556–1567 (2012).

[35] Zhipeng Chen, Jianhong Shi, and Guihua Zeng, "Object authentication based on compressive ghost imaging," Appl. Opt. **55**, 8644–8650 (2016).

[36] S. Li, F. Cropp, K. Kabra, T. J. Lane, G. Wetzstein, P. Musumeci, and D. Ratner, "Electron ghost imaging," Phys. Rev. Lett. **121**, 114801 (2018).

[37] C. Behrens, F.-J. Decker, Y. Ding, V. A. Dolgashev, J. Frisch, Z. Huang, P. Krejcik, H. Loos, A. Lutman, T. J. Maxwell, J. Turner, J. Wang, M.-H. Wang, J. Welch, and J. Wu, "Few-femtosecond time-resolved measurements of x-ray free-electron lasers," Nature Communications **5**, 3762 (2014).

[38] E. L. Saldin, E. A. Schneidmiller, and M. V. Yurkov, "Optical afterburner for an x-ray free electron laser as a tool for pump-probe experiments," Phys. Rev. ST Accel. Beams **13**, 030701 (2010).

[39] N. Hartmann, G. Hartmann, R. Heider, M. S. Wagner, M. Ilchen, J. Buck, A. O. Lindahl, C. Benko, J. Grunert, J. Krzywinski, J. Liu, A. A. Lutman, A. Marinelli, T. Maxwell, A. A. Miahnahri, S. P. Moeller, M. Planas, J. Robinson, A. K. Kazansky, N. M. Kabachnik, J. Viefhaus, T. Feurer, R. Kienberger, R. N. Coffee, and W. Helml, "Attosecond timeenergy structure of x-ray free-electron laser pulses," Nature Phot. **12**, 215 (2018).

[40] F. Christie, J. Ransch-Schulenburg, M. Vogt, Y. Ding, Z. Huang, J. Krzywinski, A. A. Lutman, T. J. Maxwell, D. Ratner, and V. A. Jhalani, "Temporal x-ray reconstruction using temporal and spectral measurements," in *Proceedings of IPAC2018* (Vancouver, Canada, 2018) p. TUPMF076.

[41] Diling Zhu, Marco Cammarata, Jan M. Feldkamp, David M. Fritz, Jerome B. Hastings, Sooheyong Lee, Henrik T. Lemke, Aymeric Robert, James L. Turner, and Yiping Feng, "A single-shot transmissive spectrometer for hard x-ray free electron lasers," Applied Physics Letters **101**, 034103 (2012).

[42] P. Emma, R. Akre, J. Arthur, R. Bionta, C. Bostedt, J. Bozek, A. Brachmann, P. Bucksbaum, R. Coffee, F.-J. Decker, Y. Ding, D. Dowell, S. Edstrom, A. Fisher, J. Frisch, S. Gilevich, J. Hastings, G. Hays, Ph. Hering, Z. Huang, R. Iverson, H. Loos, M. Messerschmidt,

A. Miahnahri, S. Moeller, H.-D. Nuhn, G. Pile, D. Ratner, J. Rzepiela, D. Schultz, T. Smith, P. Stefan, H. Tompkins, J. Turner, J. Welch, W. White, J. Wu, G. Yocky, and J. Galayda, "First lasing and operation of an angstrom-wavelength free-electron laser," Nature Photonics **4**, 641–647 (2010).

[43] 1-D FEL code used courtesy of Zhirong Huang.

[44] S. Boyd, N. Parikh, E. Chu, B. Peleato, and J. Eckstein, "Distributed optimization and statistical learning via the alternating direction method of multipliers," Foundations and Trends in Machine Learning **3**, 1–122 (2011).

[45] E. A. Schneidmiller and M. V. Yurkov, "Using the longitudinal space charge instability for generation of vacuum ultraviolet and x-ray radiation," Phys. Rev. ST Accel. Beams **13**, 110701 (2010).

[46] D. Ratner, C. Behrens, Y. Ding, Z. Huang, A. Marinelli, T. Maxwell, and F. Zhou, "Time-resolved imaging of the microbunching instability and energy spread at the linac coherent light source," Phys. Rev. ST Accel. Beams **18**, 030704 (2015).

[47] James M. Glownia, J. Cryan, J. Andreasson, A. Belkacem, N. Berrah, C. I. Blaga, C. Bostedt, J. Bozek, L. F. DiMauro, L. Fang, J. Frisch, O. Gessner, M. Gühr, J. Hajdu, M. P. Hertlein, M. Hoener, G. Huang, O. Kornilov, J. P. Marangos, A. M. March, B. K. McFarland, H. Merdji, V. S. Petrovic, C. Raman, D. Ray, D. A. Reis, M. Trigo, J. L. White, W. White, R. Wilcox, L. Young, R. N. Coffee, and P. H. Bucksbaum, "Time-resolved pump-probe experiments at the lcls," Opt. Express **18**, 17620–17630 (2010).

[48] M. Harmand, R. Coffee, M. R. Bionta, M. Chollet, D. French, D. Zhu, D. M. Fritz, H. T. Lemke, N. Medvedev, B. Ziaja, S. Toleikis, and M. Cammarata, "Achieving few-femtosecond time-sorting at hard x-ray free-electron lasers," Nature Photonics **7**, 215 (2013).

[49] F. Bencivenga, R. Cucini, F. Capotondi, A. Battistoni, R. Mincigrucci, E. Giangrisostomi, A. Gessini, M. Manfredda, I. P. Nikolov, E. Pedersoli, E. Principi, C. Svetina, P. Parisse, F. Casolari, M. B. Danailov, M. Kiskinova, and C. Masciovecchio, "Four-wave mixing experiments with extreme ultraviolet transient gratings," Nature **520**, 205 (2015).

I. AUTOCORRELATION MATRIX QUALITY

The pump-probe ghost imaging method works generally with any SASE FEL configuration, provided there is sufficient resolution to measure shot-by-shot fluctuations. However, we observe empirically that untapered, post-saturation configurations produce better reconstructions compared to an FEL in pre-saturation (Fig. 1). This is particularly surprising for the spectral approach (Fig. 1b,d), given that the Pearson correlation between the field and power autocorrelations is smaller for the post-saturation case (Section IV).

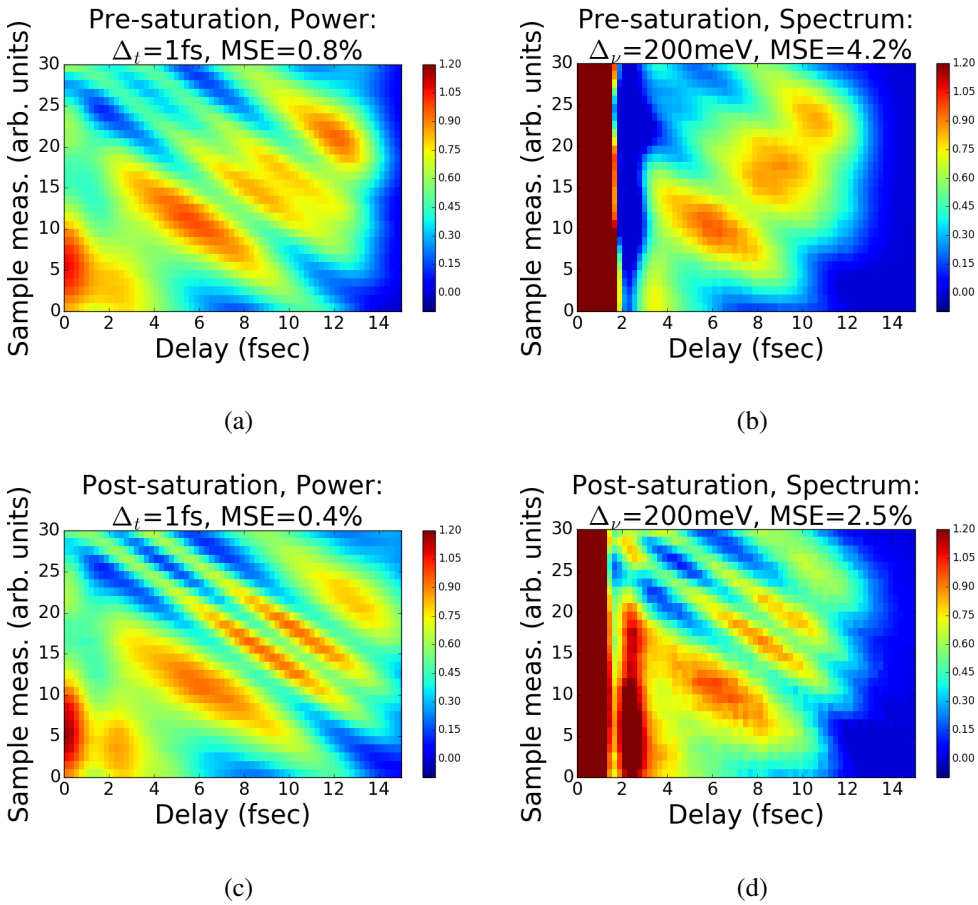

FIG. 1. Reconstructions for the four autocorrelations shown in Fig. 3. Top plots (a, b) are for pre-saturation, and bottom plots (c, d) are for post-saturation. Left plots use power, 1fs resolution, and right plots use spectrum, 200 meV resolution.

A partial explanation for the advantage at post-saturation is that shorter coherence lengths lead to sharper features in the autocorrelation, and thus better time resolution in the reconstruction. The saturated case has shorter coherence length: 1.57 fs for post-saturation vs. 1.82 fs for the pre-

saturation case. However, even taking the larger coherence length into account, the pre-saturation case still has somewhat worse reconstruction performance. To support this observation, we calculate the singular value decomposition (SVD) to check the conditioning of each matrix. Fig. 2 plots the eigenvalues for four cases, using either pre- or post-saturation FELs, and using either power or field autocorrelations. (As explained in the main paper, the field autocorrelation is used in the spectral approach.) We find that the post-saturation matrices are better conditioned than the pre-saturation matrices, and the power matrices are better conditioned than the field (spectral) matrices. We also calculate the Gram matrices of the autocorrelations (Fig. 3), which give the co-dependence of features. Fig. 1 shows the corresponding reconstructions for each of the four cases in Figs. 2 and 3. It may be possible to further improve the conditioning by manipulating the electron beam quality, e.g. by intentionally inducing the microbunching instability (MBI) [1] to reduce the number of spikes. (Examples of the resulting distorted phase space can be found in [2].) The high current spikes of an MBI-distorted beam also have the effect of reducing the FEL coherence length [3], improving the theoretical limit for the temporal resolution of PPGI.

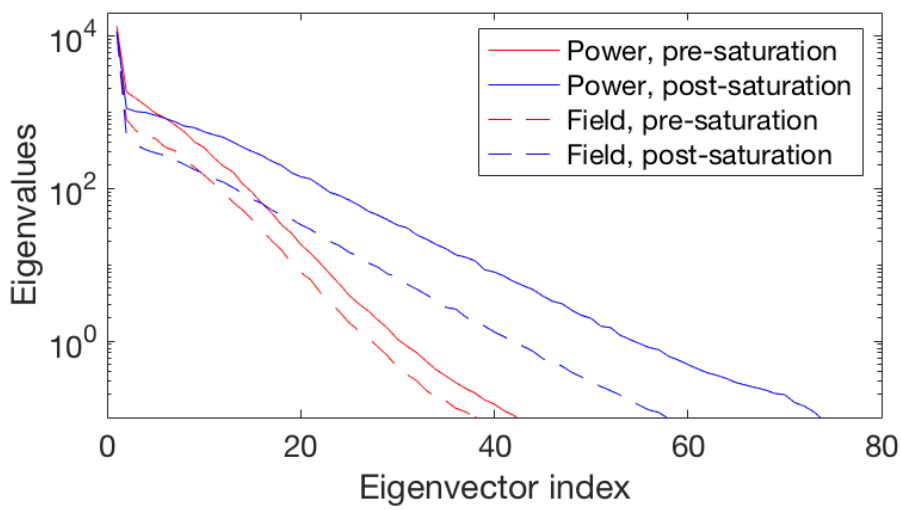

FIG. 2. SVD eigenvalues for the four cases: pre-saturation (red) vs. post-saturation (blue), and power autocorrelations (solid lines) vs. field autocorrelations (dashed lines).

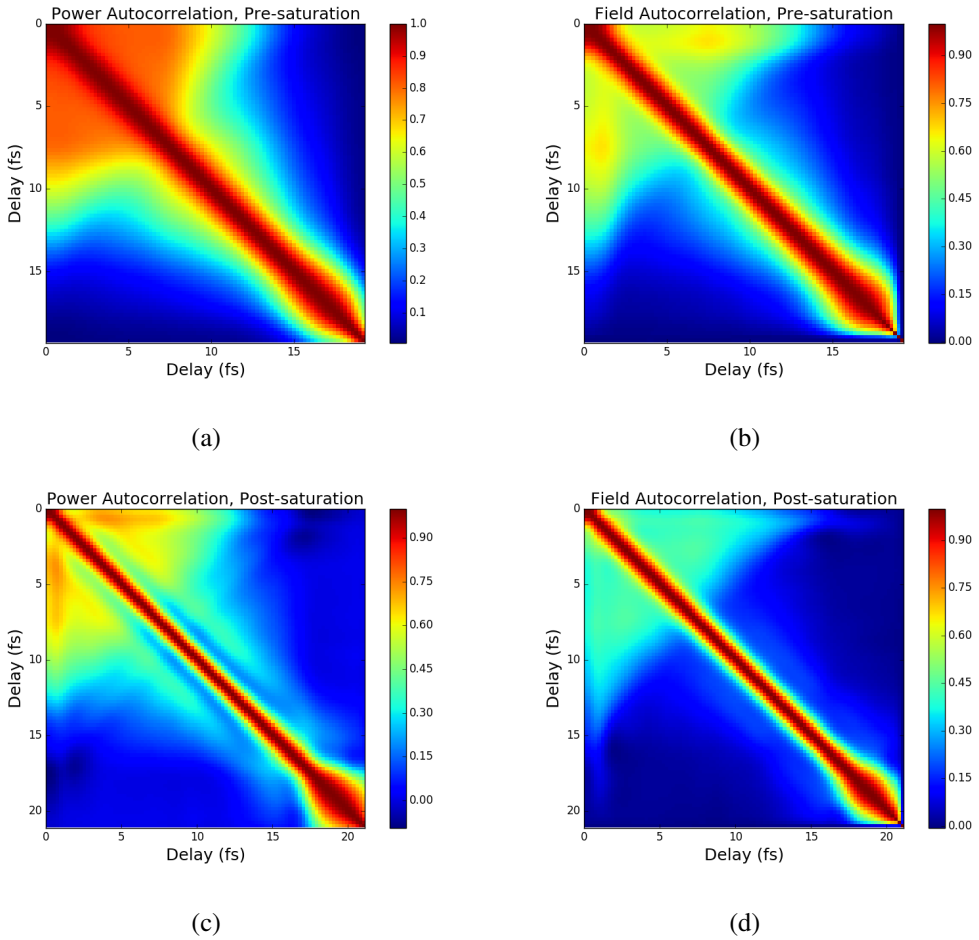

FIG. 3. Gram matrices for FELs in pre-saturation (top) and post-saturation (bottom). Matrices are calculated for the second order/power autocorrelation (left), and the first-order/field autocorrelation (right). A perfectly independent matrix would only have non-zero entries on the diagonal. For both power and field cases, the post-saturation regime (bottom plots) gives better-conditioned matrices.

II. THE FIRST VS. SECOND ORDER AUTOCORRELATION PROBLEM

For the remainder of the supplemental information, we calculate several relations between the first and second order autocorrelations. In this section, we calculate the expectation value of first and second order autocorrelations, and find a new relation that applies to fields with finite coherence lengths (Eq. 10). Section III calculates the variances for both the first and second order correlations in a general case. Section IV applies the results to the special case of Gaussian wave packets, a common model used to describe FEL pulses in the linear (pre-saturation) regime [4]. We compare these results to 1-D FEL simulations and confirm that the analytical equations are good

approximations for FELs.

Let $f(t)$ be a random process that has the following form

$$f(t) = e(t)w(t), \tag{1}$$

where $e(t)$ is a stationary complex-valued stochastic process [5], and $w(t)$ denotes a (deterministic) real window function (e.g. equal to 1 for $0 < t < T$ and zero otherwise). Related to the fluctuational part of the field $e(t)$ is a correlation function $K(\tau)$,

$$K(\tau) = \langle e(t)\, e^*(t-\tau)\rangle, \tag{2}$$

where the angular brackets denote the ensemble average.

Following Ref. [4], we define

$$A^{(f)}(\tau) = \int dt f(t) f^*(t-\tau), \qquad A^{(p)}(\tau) = \int dt |f(t)|^2 |f(t-\tau)|^2, \tag{3}$$

(here we ignore the normalization factor).

Let us calculate $\langle |A^{(f)}(\tau)|^2\rangle$. We have

$$\begin{aligned}\langle |A^{(f)}(\tau)|^2\rangle &= \langle \int dt\, dt' f(t) f^*(t-\tau) f^*(t') f(t'-\tau)\rangle \\ &= \int dt\, dt' w(t) w(t-\tau) w(t') w(t'-\tau) \langle e(t) e^*(t-\tau) e^*(t') e(t'-\tau)\rangle.\end{aligned} \tag{4}$$

The correlator in this equation can be easily calculated (see also Ref. [6]):

$$\begin{aligned}\langle e(t)\, e^*(t-\tau)\, e^*(t')\, e(t'-\tau)\rangle &= \langle e(t)\, e^*(t-\tau)\rangle \langle e^*(t')\, e(t'-\tau)\rangle + \langle e(t)\, e^*(t')\rangle \langle e^*(t-\tau)\, e(t'-\tau)\rangle \\ &= |K(\tau)|^2 + \left|K(t-t')\right|^2.\end{aligned} \tag{5}$$

Using this correlator we obtain

$$\langle |A^{(f)}(\tau)|^2\rangle = \int dt\, dt' w(t) w(t-\tau) w(t') w(t'-\tau) \left[|K(\tau)|^2 + \left|K(t-t')\right|^2\right]. \tag{6}$$

We are interested in values of τ much larger than the correlation time, $\tau \gg \tau_{\text{corr}}$. In this limit $K(\tau) \to 0$ and can be neglected. Changing the integration variable $t' = t - \xi$ we find

$$\langle |A^{(f)}(\tau)|^2\rangle = \int dt\, d\xi w(t) w(t-\tau) w(t-\xi) w(t-\xi-\tau)\, |K(\xi)|^2. \tag{7}$$

We now assume that $w(t)$ is a broad function—it varies on the time scale much larger than τ_{corr}. We then can neglect ξ in the argument of w in this integral, because the dominant contribution to

the integral comes from the region where $\xi \sim \tau_{\rm corr}$ which by assumption is much smaller that the time scale of function w. We obtain

$$\langle |A^{(f)}(\tau)|^2 \rangle = \left(\int dt\, w(t)^2 w(t-\tau)^2 \right) \left(\int d\xi\, |K(\xi)|^2 \right). \tag{8}$$

We now calculate $\langle A^{(f)}(\tau) \rangle$, again using the correlator (5):

$$\begin{aligned} \langle A^{(p)}(\tau) \rangle &= \int dt w(t)^2 w(t-\tau)^2 \langle e(t) e^*(t) e(t-\tau) e^*(t-\tau) \rangle \\ &= \int dt w(t)^2 w(t-\tau)^2 \left[|K(\tau)|^2 + K_0^2 \right] \approx K_0^2 \int dt w(t)^2 w(t-\tau)^2, \end{aligned} \tag{9}$$

where $K_0 = |K(0)|$. As above, we neglected the $K(\tau)$ term. After that, comparing the result with Eq. (8) we conclude that

$$\langle A^{(p)}(\tau) \rangle = \frac{M}{T} \langle |A^{(f)}(\tau)|^2 \rangle \tag{10}$$

where

$$M = T K_0^2 \left(\int d\xi\, |K(\xi)|^2 \right)^{-1} \tag{11}$$

is the number of modes in the pulse.

III. VARIANCE AND CORRELATION

We will now calculate the variance of the two functions, $\mathrm{Var}(|A^{(f)}(\tau)|^2)$ and $\mathrm{Var}(A^{(p)}(\tau))$,

$$\mathrm{Var}(|A^{(f)}(\tau)|^2) = \langle |A^{(f)}(\tau)|^4 \rangle - \langle |A^{(f)}(\tau)|^2 \rangle^2, \qquad \mathrm{Var}(A^{(p)}(\tau)) = \langle A^{(p)}(\tau)^2 \rangle - \langle A^{(p)}(\tau) \rangle^2 . \tag{12}$$

Let us start with $\langle |A^{(f)}(\tau)|^4 \rangle$,

$$\begin{aligned} \langle |A^{(f)}(\tau)|^4 \rangle = &= \langle \int dt\, dt'\, dt''\, dt''' f(t) f^*(t-\tau) f^*(t') f(t'-\tau) f(t'') f^*(t''-\tau) f^*(t''') f(t'''-\tau) \rangle \\ &= \int dt\, dt'\, dt''\, dt''' w(t) w(t-\tau) w(t') w(t'-\tau) w(t'') w(t''-\tau) w(t''') w(t'''-\tau) \\ &\times \langle e(t) e^*(t-\tau) e^*(t') e(t'-\tau) e(t'') e^*(t''-\tau) e^*(t''') e(t'''-\tau) \rangle. \end{aligned} \tag{13}$$

Calculating the 8-correlator of the e field

$$\langle e(t) e^*(t-\tau) e^*(t') e(t'-\tau) e(t'') e^*(t''-\tau) e^*(t''') e(t'''-\tau) \rangle \tag{14}$$

we will have 4!=24 terms. We can drop most of them because they give a result that is small by the ratio $\tau_{\rm corr}/T$, see Appendix A. Out of 24 only two terms should be kept:

$$|K(t-t')|^2|K(t''-t''')|^2 + |K(t-t''')|^2|K(t'-t''')|^2 \,. \tag{15}$$

After putting these terms in Eq. (13) and integrating over times, each of these terms gives the same contribution to $\langle|A^{(f)}(\tau)|^4\rangle$, and one of them cancels $\langle|A^{(f)}(\tau)|^2\rangle^2$. We end with the following result

$$\mathrm{Var}(|A^{(f)}(\tau)|^2) = \langle|A^{(f)}(\tau)|^2\rangle^2, \tag{16}$$

which means that the standard deviation of $|A^{(f)}(\tau)|^2$ is equal to its average value squared. In Appendix A we also calculate corrections to this expression of the order of $\tau_{\rm corr}/T$ that give a better agreement with the simulations. These corrections are given by Eq. (A12).

For the variance $\mathrm{Var}(A^{(p)}(\tau))$ we need to calculate $\langle A^{(p)}(\tau)^2\rangle$

$$\begin{aligned}\langle A^{(p)}(\tau)^2\rangle = &\int dt\, dt'\; w(t)^2 w(t-\tau)^2 w(t')^2 w(t'-\tau)^2 \\ &\times \langle e(t)e^*(t)e(t-\tau)e^*(t-\tau)e(t')e^*(t')e(t'-\tau)e^*(t'-\tau)\rangle \,.\end{aligned} \tag{17}$$

This correlator is computed in Appendix B. The result is given by Eq. (B6).

Finally, we calculate the following correlation factor

$$\begin{aligned}\mathrm{corr} &= \langle(|A^{(f)}(\tau)|^2 - \langle|A^{(f)}(\tau)|^2\rangle)(A^{(p)}(\tau) - \langle A^{(p)}(\tau)\rangle)\rangle \\ &= \langle|A^{(f)}(\tau)|^2 A^{(p)}(\tau)\rangle - \langle|A^{(f)}(\tau)|^2\rangle\langle A^{(p)}(\tau)\rangle \,.\end{aligned} \tag{18}$$

Let's calculate the first term

$$\begin{aligned}\langle|A^{(f)}(\tau)|^2 A^{(p)}(\tau)\rangle = &\int dt\, dt'\, dt'' w(t)w(t-\tau)w(t')w(t'-\tau)w(t'')^2 w(t''-\tau)^2 \\ &\times \langle e(t)e^*(t-\tau)e^*(t')e(t'-\tau)e(t'')e^*(t'')e(t''-\tau)e^*(t''-\tau)\rangle \,.\end{aligned} \tag{19}$$

We need to average

$$\langle e(t)e^*(t-\tau)e^*(t')e(t'-\tau)e(t'')e^*(t'')e(t''-\tau)e^*(t''-\tau)\rangle. \tag{20}$$

This term is calculated in Appendix C. The first term cancels the product of averaged values in Eq. (18). The final result is given by Eq. (C28).

Finally, we want to calculate the Pearson correlation coefficient, $C_p(\tau)$, given by

$$C_p \equiv \frac{\langle|A^{(f)}(\tau)|^2 A^{(p)}(\tau)\rangle}{\mathrm{Var}(|A^{(f)}(\tau)|^2)\mathrm{Var}(A^{(p)}(\tau))} \,. \tag{21}$$

IV. THE MODEL OF GAUSSIAN PULSES

We now take a specific case of Gaussian pulses that is a standard approximation for SASE FEL pulses [**?**]. Consider a random process where $e(t)$ is a collection of random Gaussian pulses

$$e(t) = \sum_i e^{-(t-t_i)^2/2\sigma^2 + i\phi_i} \,. \tag{22}$$

where t_i are random uncorrelated times uniformly distributed over the interval $[0, T]$ with the probability dt_i/T, coherence length σ, and ϕ_i are random phases. The correlation function (2) is

$$K(\tau) = \sum_{i,j} \langle e^{-(t-t_i)^2/2\sigma^2 + i\phi_i} e^{-(t-\tau-t_j)^2/2\sigma^2 - i\phi_j} \rangle \,. \tag{23}$$

Because the phases are not correlated, only terms with $i = j$ survive,

$$\begin{aligned} K(\tau) &= \frac{1}{T} \sum_i \int_0^T dt_i e^{-(t-t_i)^2/2\sigma^2} e^{-(t-\tau-t_i)^2/2\sigma^2} \\ &\approx \frac{N}{T} \int_{-\infty}^{\infty} dt_i e^{-(t-t_i)^2/2\sigma^2} e^{-(t-\tau-t_i)^2/2\sigma^2} \;=\; \sqrt{\pi}\nu\sigma e^{-\tau^2/4\sigma^2}, \end{aligned} \tag{24}$$

where ν is the number of pulses per unit time. We need the following integral

$$\int_{-\infty}^{\infty} d\xi \, |K(\xi)|^2 = \nu^2 \pi \sigma^2 \int_{-\infty}^{\infty} d\xi e^{-\tau^2/2\sigma^2} = 2^{1/2} \pi^{3/2} \sigma^3 \nu^2 \,. \tag{25}$$

We then have from Eqs. (8) and (9)

$$\langle |A^{(f)}(\tau)|^2 \rangle = 2^{1/2} \pi^{3/2} \sigma^3 \nu^2 |T - \tau|, \qquad \langle A^{(p)}(\tau) \rangle = \nu^2 \pi \sigma^2 |T - \tau|. \tag{26}$$

The number of modes (11) in the pulse is

$$M = \frac{T}{\sqrt{2\pi}\,\sigma} \,. \tag{27}$$

We now calculate M_1 using Eq. (B7),

$$\begin{aligned} M_1 &= T\,|K_0|^4 \left(\int d\xi \, |K(\xi)|^4 \right)^{-1} \\ &= T \left(\int d\xi e^{-\xi^2/\sigma^2} \right)^{-1} = \frac{T}{\sigma\sqrt{\pi}} \,. \end{aligned} \tag{28}$$

We have two equations for the variances:

$$\sqrt{\mathrm{Var}(|A^{(f)}(\tau)|^2)} = \langle |A^{(f)}(\tau)|^2 \rangle = (T - \tau)|K_0|^2 \frac{T}{M} \tag{29}$$

and

$$\mathrm{Var}(A^{(p)}(\tau)) = |K_0|^4 T \left[\left(\frac{2}{M} + \frac{1}{M_1} \right) (T-\tau) h(T-\tau) + \frac{1}{M_1} (T-2\tau)\, h\,(T-2\tau) \right]. \tag{30}$$

Let us calculate M_2 for the correlation function given by Eq. (24),

$$\frac{T^2}{M_2^2} = K_0^{-3} \int d\xi_1\, d\xi_2 K(\xi_1) K(\xi_2) K(-\xi_1-\xi_2) = \int d\xi_1\, d\xi_2 e^{-\xi_1^2/4\sigma^2} e^{-\xi_2^2/4\sigma^2} e^{-(\xi_1+\xi_2)^2/4\sigma^2} = \frac{4\pi\sigma^2}{\sqrt{3}} \tag{31}$$

which gives

$$M_2 = \frac{3^{1/4} T}{2\sqrt{\pi}\sigma}. \tag{32}$$

For the number M_3 we find

$$\frac{1}{M_3^3} = 4\pi^{3/2} \frac{\sigma^3}{T^3}. \tag{33}$$

Plugging these results into the expressions for the correlators we compare to simulations of Gaussian wavepackets in Figs. 4-6.

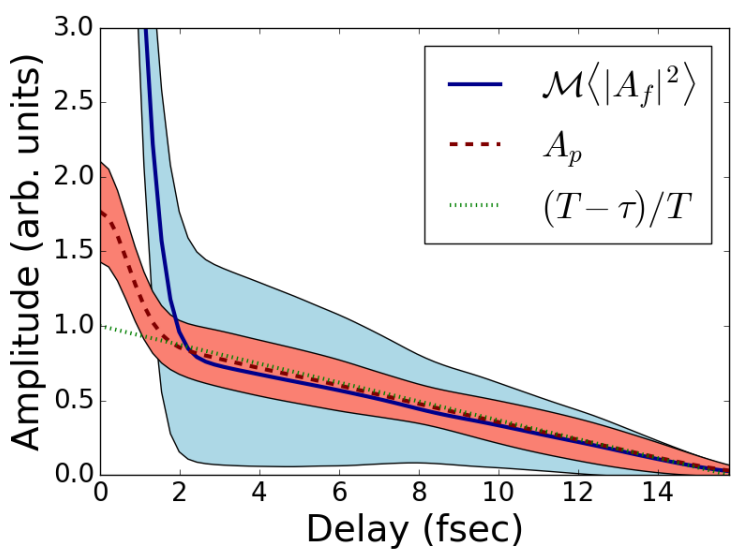

FIG. 4. Comparison of theory (Eq. 10) and simulations of an FEL in pre-saturation. Shaded areas show standard deviation of fluctuations for the simulations.

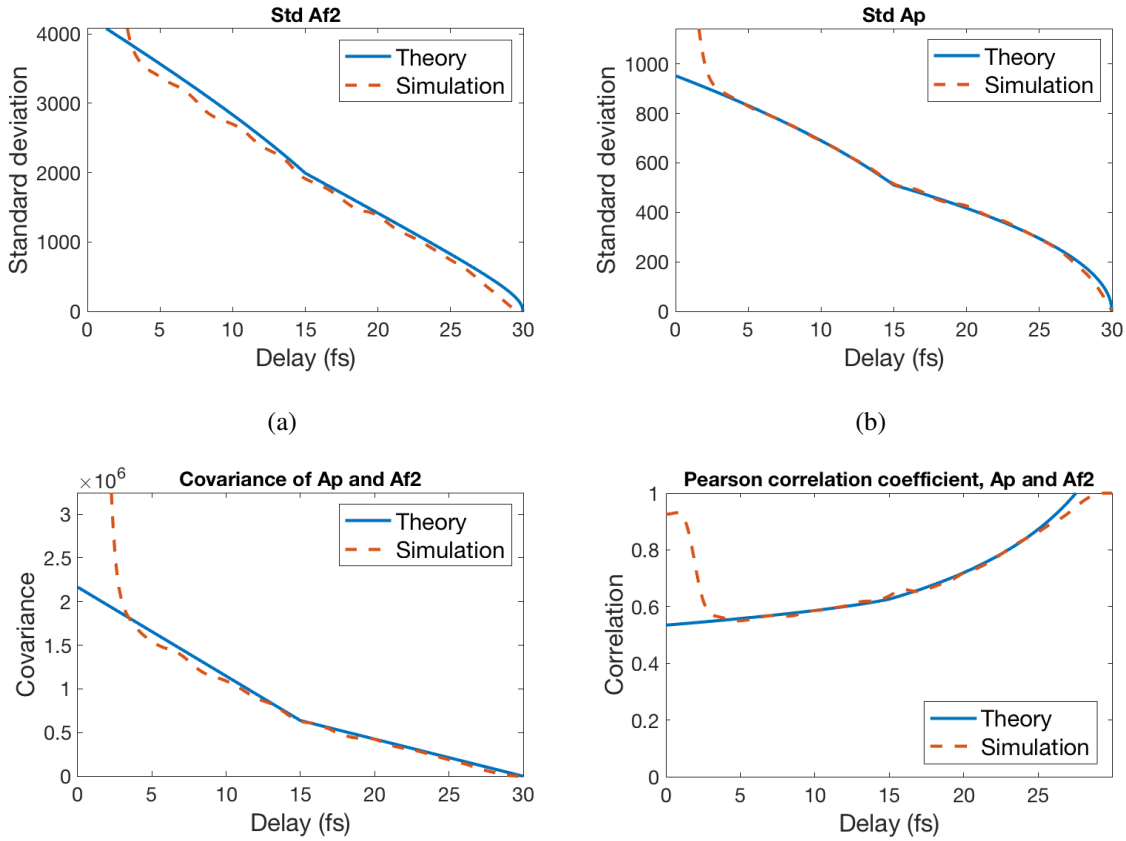

(a) (b) (c) (d)

FIG. 5. Comparison of analytical expressions (solid blue line) with simulations of Gaussian wavepackets (dashed red line). Plots show standard deviation of $|A^f|^2$ (top left), standard deviation of A^p (top right), covariance of $|A^f|^2$ and A^p (bottom left), and pearson correlation coefficient of $|A^f|^2$ and A^p (bottom right).

[1] E. A. Schneidmiller and M. V. Yurkov, "Using the longitudinal space charge instability for generation of vacuum ultraviolet and x-ray radiation," Phys. Rev. ST Accel. Beams **13**, 110701 (2010).

[2] D. Ratner, C. Behrens, Y. Ding, Z. Huang, A. Marinelli, T. Maxwell, and F. Zhou, "Time-resolved imaging of the microbunching instability and energy spread at the linac coherent light source," Phys. Rev. ST Accel. Beams **18**, 030704 (2015).

[3] A. A. Zholents and W. M. Fawley, "Proposal for intense attosecond radiation from an x-ray free-electron laser," Phys. Rev. Lett. **92**, 224801 (2004).

[4] Kwang-Je Kim, Zhirong Huang, and Ryan Lindberg, *Synchrotron radiation and free-electron lasers*

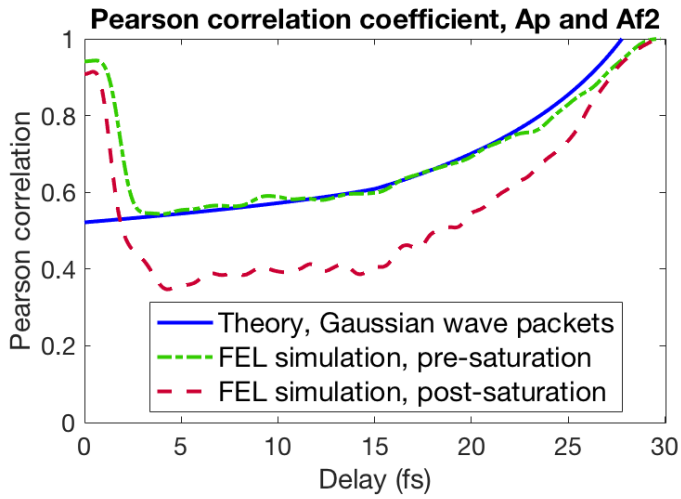

(a)

FIG. 6. Comparison of pearson correlation between $|A^f|^2$ and A^p for analytical expression (solid blue line) and 1-D FEL simulations [a] in the pre-saturation (dot-dashed green line) and post-saturation (dashed red line) regimes.

[a] 1-D FEL code used courtesy of Zhirong Huang

(Cambridge University Press, 2017).

[5] M. S. Zolotorev and G. V. Stupakov, "Spectral fluctuations of incoherent radiation and measurement of longitudinal bunch profile," in *Proceedings of the 1997 Particle Accelerator Conference* (Vancouver, Canada, 1997).

[6] D. R. Cox and H. D. Miller, *The Theory of Stochastic Processes* (John Wiley Inc., 1965).

Appendix A: Calculation of $\langle |A^{(f)}(\tau)|^4 \rangle$

In calculation of the correlators we need to pair e and e^* in the product of the fields and add the results. We show the pairing by lines connecting the corresponding terms.

Term 1:

$$e(t) \quad e^*(t-\tau) \quad e^*(t') \quad e(t'-\tau) \quad e(t'') \quad e^*(t''-\tau) \quad e^*(t''') \quad e(t'''-\tau)$$

This term is

$$|K(t-t')|^2 |K(t''-t''')|^2 \tag{A1}$$

After integration over all times in Eq. (13) this term gives a contribution of the order of

$$\sim K_0^4 T^2 \tau_{\rm corr}^2 \tag{A2}$$

This term will cancel $\langle |A^{(f)}(\tau)|^2 \rangle^2$.

Term 2:

$$e(t)\ \ e^*(t-\tau)\ \ e^*(t')\ \ e(t'-\tau)\ \ e(t'')\ \ e^*(t''-\tau)\ \ e^*(t''')\ \ e(t'''-\tau)$$

This term is equal to

$$K(t-t')K(t''-t+\tau)K(t'-t'''-\tau)K(t'''-t'') \tag{A3}$$

From the first and the last term it follows that $|t-t'| \lesssim \tau_{\rm corr}$ and $|t'''-t''| \lesssim \tau_{\rm corr}$. Introduce new variables $\xi_1 = t-t'$, $\xi_2 = t'''-t''$ and $\xi_3 = t''-t+\tau$, then the third argument is $t'-t'''-\tau = -(\xi_1+\xi_2+\xi_3)$. Integration over each of the varibles ξ_1, ξ_2, ξ_3 is limited by the interval $\tau_{\rm corr}$, integration over the fourth variable will go over the interval $\sim T$. Hence the result will be of the order of

$$K_0^4 T \tau_{\rm corr}^3 \tag{A4}$$

which is much smaller than (A2).

Term 3:

$$e(t)\ \ e^*(t-\tau)\ \ e^*(t')\ \ e(t'-\tau)\ \ e(t'')\ \ e^*(t''-\tau)\ \ e^*(t''')\ \ e(t'''-\tau)$$

This term is equal to

$$K(t-t')K(t'''-t)K(t'-t'')K(t''-t''') \tag{A5}$$

This term will be of the order of $K_0^4 T \tau_{\rm corr}^3$.

Term 4:

$$e(t)\ \ e^*(t-\tau)\ \ e^*(t')\ \ e(t'-\tau)\ \ e(t'')\ \ e^*(t''-\tau)\ \ e^*(t''')\ \ e(t'''-\tau)$$

This term is equal to

$$K(t-t''+\tau)K(t'-t)K(t'''-t'-\tau)K(t''-t''') \tag{A6}$$

This term will be of the order of $K_0^4 T \tau_{\rm corr}^3$.

Term 5:

$$e(t)\quad e^*(t-\tau)\quad e^*(t')\quad e(t'-\tau)\quad e(t'')\quad e^*(t''-\tau)\quad e^*(t''')\quad e(t'''-\tau)$$

This term is equal to

$$K(t-t''+\tau)K(t''-t+\tau)K(t'''-t'-\tau)K(t'-t'''-\tau) \tag{A7}$$

This term is exponentially small and will be neglected.

Term 6:

$$e(t)\quad e^*(t-\tau)\quad e^*(t')\quad e(t'-\tau)\quad e(t'')\quad e^*(t''-\tau)\quad e^*(t''')\quad e(t'''-\tau)$$

This term is equal to

$$K(t-t''+\tau)K(t'''-t)K(t''-t')K(t'-t'''-\tau) \tag{A8}$$

This term will be of the order of $K_0^4 T\tau_{\text{corr}}^3$.

Term 7:

$$e(t)\quad e^*(t-\tau)\quad e^*(t')\quad e(t'-\tau)\quad e(t'')\quad e^*(t''-\tau)\quad e^*(t''')\quad e(t'''-\tau)$$

This term is equal to

$$K(t-t''')K(t'-t)K(t''-t')K(t'''-t'') \tag{A9}$$

This term will be of the order of $K_0^4 T\tau_{\text{corr}}^3$.

Term 8:

$$e(t)\quad e^*(t-\tau)\quad e^*(t')\quad e(t'-\tau)\quad e(t'')\quad e^*(t''-\tau)\quad e^*(t''')\quad e(t'''-\tau)$$

This term is equal to

$$K(t-t''')K(t''-t+\tau)K(t'''-t'-\tau)K(t'-t'') \tag{A10}$$

This term will be of the order of $K_0^4 T\tau_{\text{corr}}^3$.

Term 9:

$$e(t)\quad e^*(t-\tau)\quad e^*(t')\quad e(t'-\tau)\quad e(t'')\quad e^*(t''-\tau)\quad e^*(t''')\quad e(t'''-\tau)$$

This term is equal to

$$K(t-t''')K(t'''-t)K(t''-t')K(t'-t'') = |K(t-t''')|^2|K(t'-t'')|^2 \tag{A11}$$

The terms 1 and 9 result in the expression (16). The terms 2, 3, 4, 6, 7 and 8 can also be calculated. For the rectangular window function $w(t)$ they give the following result

$$\frac{1}{M_3^3} K_0^4 T^3 \left[4(T-2\tau)h(T-2\tau) + 2(T-\tau)h(T-\tau)\right], \tag{A12}$$

where the number M_3 is defined by the following equation

$$\frac{1}{M_3^3} = \frac{1}{K_0^4 T^3} \int d\xi_1\, d\xi_2\, d\xi_3\, K(\xi_1)K(\xi_2)K(\xi_3)K(-\xi_1-\xi_2-\xi_3). \tag{A13}$$

Appendix B: Calculation of $\langle A^{(p)}(\tau)^2\rangle$

To calculate this we need to correlate pairs of the field e and e^* in different combinations. Let's start:

$$e(t)\ e^*(t)\ e(t-\tau)\ e^*(t-\tau)\ e(t')\ e^*(t')\ e(t'-\tau)\ e^*(t'-\tau) \qquad = |K(0)|^4$$

$$e(t)\ e^*(t)\ e(t-\tau)\ e^*(t-\tau)\ e(t')\ e^*(t')\ e(t'-\tau)\ e^*(t'-\tau) \quad = |K(0)|^2|K(t-t'-\tau)|^2$$

$$e(t)\ e^*(t)\ e(t-\tau)\ e^*(t-\tau)\ e(t')\ e^*(t')\ e(t'-\tau)\ e^*(t'-\tau) \quad = |K(0)|^2|K(t-t')|^2$$

$$e(t)\ e^*(t)\ e(t-\tau)\ e^*(t-\tau)\ e(t')\ e^*(t')\ e(t'-\tau)\ e^*(t'-\tau) \quad = |K(0)|^2|K(t-t')|^2$$

$$e(t)\ e^*(t)\ e(t-\tau)\ e^*(t-\tau)\ e(t')\ e^*(t')\ e(t'-\tau)\ e^*(t'-\tau) \qquad = |K(t-t')|^4$$

$$e(t)\ e^*(t)\ e(t-\tau)\ e^*(t-\tau)\ e(t')\ e^*(t')\ e(t'-\tau)\ e^*(t'-\tau) \quad = [K(t-t')]^2 K(t'-t+\tau)K(t'-t-\tau)$$

$$e(t)\ e^*(t)\ e(t-\tau)\ e^*(t-\tau)\ e(t')\ e^*(t')\ e(t'-\tau)\ e^*(t'-\tau) \quad = [K(t'-t)]^2 K(t-t'+\tau)K(t-t'-\tau)$$

$$e(t)\ e^*(t)\ e(t-\tau)\ e^*(t-\tau)\ e(t')\ e^*(t')\ e(t'-\tau)\ e^*(t'-\tau) \qquad = |K(0)|^2|K(t-t'+\tau)|^2$$

$$e(t)\ e^*(t)\ e(t-\tau)\ e^*(t-\tau)\ e(t')\ e^*(t')\ e(t'-\tau)\ e^*(t'-\tau) \qquad = |K(t-t'+\tau)|^2|K(t-t'-\tau)|^2$$

We do not show terms that turns out to be proportional to $K(\tau)$ and can be neglected right away in the limit $\tau \gg \tau_{\text{corr}}$.

The first term $|K(0)|^4$ cancels $\langle A^{(p)}(\tau)\rangle^2$, see Eq. (9).

The second term is $|K(0)|^2|K(t-t'-\tau)|^2$ which gives

$$\begin{aligned} &K_0^2 \int dt\, dt'\, w(t)^2 w(t-\tau)^2 w(t')^2 w(t'-\tau)^2 |K(t-t'-\tau)|^2 \\ &\approx K_0^2 \int dt\, w(t)^2 w(t-\tau)^4 w(t-2\tau)^2 \int d\xi\, |K(\xi)|^2 \end{aligned} \tag{B1}$$

Then we have 2 terms $|K(0)|^2|K(t-t')|^2$ which give

$$\begin{aligned} &2K_0^2 \int dt\, dt'\; w(t)^2 w(t-\tau)^2 w(t')^2 w(t'-\tau)^2 |K(t-t')|^2 \\ &\approx 2K_0^2 \int dt\, w(t)^4 w(t-\tau)^4 \int d\xi\, |K(\xi)|^2 \end{aligned} \tag{B2}$$

Then we have $|K(t-t')|^4$ which gives

$$\begin{aligned} &\int dt\, dt'\; w(t)^2 w(t-\tau)^2 w(t')^2 w(t'-\tau)^2 |K(t-t')|^4 \\ &\approx \int dt\, w(t)^4 w(t-\tau)^4 \int d\xi\, |K(\xi)|^4 \end{aligned} \tag{B3}$$

The next two terms can be neglected.

The next term is $|K(0)|^2|K(t-t'+\tau)|^2$ which gives

$$\begin{aligned} &K_0^2 \int dt\, dt'\; w(t)^2 w(t-\tau)^2 w(t')^2 w(t'-\tau)^2 |K(t-t'+\tau)|^2 \\ &\approx K_0^2 \int dt\, w(t)^4 w(t-\tau)^2 w(t+\tau)^2 \int d\xi\, |K(\xi)|^2 \end{aligned} \tag{B4}$$

And finally we have $|K(t-t'+\tau)|^2|K(t-t'-\tau)|^2$ which gives

$$\begin{aligned} &\int dt\, dt'\; w(t)^2 w(t-\tau)^2 w(t')^2 w(t'-\tau)^2 |K(t-t'+\tau)|^2 |K(t-t'-\tau)|^2 \\ &\approx \int dt\, w(t)^4 w(t-\tau)^2 w(t+\tau)^2 \int d\xi\, |K(\xi)|^2 |K(\xi-2\tau)|^2 \end{aligned} \tag{B5}$$

This term is small.

This will give the following expression for the rectangular function $w(t)$

$$\mathrm{Var}(A^{(p)}(\tau)) = K_0^4 T \left[\left(\frac{2}{M} + \frac{1}{M_1} \right) (T-\tau) h(T-\tau) + \frac{2}{M} (T-2\tau)\, h\,(T-2\tau) \right] \tag{B6}$$

where

$$M_1 = T\, |K_0|^4 \left(\int d\xi\, |K(\xi)|^4 \right)^{-1} \tag{B7}$$

and h is the step function.

Appendix C: Calculation of $\langle |A^{(f)}(\tau)|^2 A^{(p)}(\tau) \rangle$

<u>Term 1</u>:

$$e(t)\quad e^*(t-\tau)\quad e^*(t')\quad e(t'-\tau)\quad e(t'')\quad e^*(t'')\quad e(t''-\tau)\quad e^*(t''-\tau)$$

This term is equal to

$$|K(t-t')|^2 K_0^2 \tag{C1}$$

After integration over all times this term is of the order of

$$K_0^4 T^2 \tau_{\text{corr}} \tag{C2}$$

It is relatively large, but it will be canceled by $\langle |A^{(f)}(\tau)|^2\rangle\langle A^{(p)}(\tau)\rangle$, so we will need to keep terms of a smaller order.

Term 2:

$$e(t)\quad e^*(t-\tau)\quad e^*(t')\quad e(t'-\tau)\quad e(t'')\quad e^*(t'')\quad e(t''-\tau)\quad e^*(t''-\tau)$$

This term is equal to

$$K(t-t')K(t''-t+\tau)K(t'-t''-\tau)K_0 \tag{C3}$$

This term will be of the order of $K_0^4 T\tau_{\text{corr}}^2$, we need to keep it.

Term 3:

$$e(t)\quad e^*(t-\tau)\quad e^*(t')\quad e(t'-\tau)\quad e(t'')\quad e^*(t'')\quad e(t''-\tau)\quad e^*(t''-\tau)$$

This term is equal to

$$K(t-t')K(t''-t)K(t'-t'')K_0 \tag{C4}$$

This term will be of the order of $K_0^4 T\tau_{\text{corr}}^2$, so we need to keep it.

Term 4:

$$e(t)\quad e^*(t-\tau)\quad e^*(t')\quad e(t'-\tau)\quad e(t'')\quad e^*(t'')\quad e(t''-\tau)\quad e^*(t''-\tau)$$

This term is equal to

$$K(t-t'')K(t'-t)K(t''-t')K_0 \tag{C5}$$

This term will be of the order of $K_0^4 T\tau_{\text{corr}}^2$, so we need to keep it.

Term 5:

$$e(t)\quad e^*(t-\tau)\quad e^*(t')\quad e(t'-\tau)\quad e(t'')\quad e^*(t'')\quad e(t''-\tau)\quad e^*(t''-\tau)$$

This term is equal to

$$K(t-t'')K(t''-t+\tau)K(t''-t'-\tau)K(t'-t'') \tag{C6}$$

This term is negligible. When we introduce variables $\xi_1 = t - t''$ and $\xi_2 = t' - t''$ it becomes

$$K(\xi_1)K(-\xi_1+\tau)K(-\xi_2-\tau)K(\xi_2) \tag{C7}$$

Since $|\xi_1|, |\xi_2| \sim \tau_{\text{corr}}$, the two middle terms are exponentially small.

<u>Term 6</u>:

$$e(t) \quad e^*(t-\tau) \quad e^*(t') \quad e(t'-\tau) \quad e(t'') \quad e^*(t'') \quad e(t''-\tau) \quad e^*(t''-\tau)$$

This term is equal to

$$K(t-t'')K(t''-t)K(t''-t')K(t'-t'') = |K(t-t'')|^2|K(t''-t')|^2 \tag{C8}$$

This term will be of the order of $K_0^4 T\tau_{\text{corr}}^2$, so we keep it.

<u>Term 7</u>:

$$e(t) \quad e^*(t-\tau) \quad e^*(t') \quad e(t'-\tau) \quad e(t'') \quad e^*(t'') \quad e(t''-\tau) \quad e^*(t''-\tau)$$

This term is equal to

$$K(t-t''+\tau)K(t'-t)K(t''-t'-\tau)K_0 \tag{C9}$$

This term will be of the order of $K_0^4 T\tau_{\text{corr}}^2$, so we keep it.

<u>Term 8</u>:

$$e(t) \quad e^*(t-\tau) \quad e^*(t') \quad e(t'-\tau) \quad e(t'') \quad e^*(t'') \quad e(t''-\tau) \quad e^*(t''-\tau)$$

This term is equal to

$$K(t-t''+\tau)K(t''-t+\tau)K(t''-t'-\tau)K(t'-t''-\tau) \tag{C10}$$

This term is exponentially small, so we neglect it.

<u>Term 9</u>:

$$e(t) \quad e^*(t-\tau) \quad e^*(t') \quad e(t'-\tau) \quad e(t'') \quad e^*(t'') \quad e(t''-\tau) \quad e^*(t''-\tau)$$

This term is equal to

$$K(t-t''+\tau)K(t''-t)K(t''-t')K(t'-t''-\tau) \tag{C11}$$

This term is exponentially small, so we neglect it.

We now finish the calculation by doing integrations over the time variables.

Term 2:

$$\int dt\, dt'\, dt'' w(t)w(t-\tau)w(t')w(t'-\tau)w(t'')^2 w(t''-\tau)^2 \\ \times K(t-t')K(t''-t+\tau)K(t'-t''-\tau)K_0 \tag{C12}$$

Use new variables $\xi_1 = t - t'$, $\xi_2 = t'' - t + \tau$

$$\approx K_0 \int dt'\, w(t')^2 w(t'-\tau)^4 w(t'-2\tau)^2 \int d\xi_1\, d\xi_2 K(\xi_1)K(\xi_2)K(-\xi_1-\xi_2) \tag{C13}$$

Term 3:

$$\int dt\, dt'\, dt'' w(t)w(t-\tau)w(t')w(t'-\tau)w(t'')^2 w(t''-\tau)^2 \\ \times K(t-t')K(t''-t)K(t'-t'')K_0 \tag{C14}$$

Use new variables $\xi_1 = t - t'$, $\xi_2 = t'' - t$

$$\approx K_0 \int dt'\, w(t')^4 w(t'-\tau)^4 \int d\xi_1\, d\xi_2 K(\xi_1)K(\xi_2)K(-\xi_1-\xi_2) \tag{C15}$$

Term 4:

$$\int dt\, dt'\, dt'' w(t)w(t-\tau)w(t')w(t'-\tau)w(t'')^2 w(t''-\tau)^2 \\ \times K(t-t'')K(t'-t)K(t''-t')K_0 \tag{C16}$$

Use new variables $\xi_1 = t - t''$, $\xi_2 = t' - t$

$$K_0 \int dt'' w(t'')^4 w(t''-\tau)^4 \int d\xi_1\, d\xi_2\, K(\xi_1)K(\xi_2)K(-\xi_1-\xi_2) \tag{C17}$$

Term 6:

$$\int dt\, dt'\, dt'' w(t)w(t-\tau)w(t')w(t'-\tau)w(t'')^2 w(t''-\tau)^2 \\ \times |K(t-t'')|^2 |K(t''-t')|^2 \tag{C18}$$

Use new variables $\xi_1 = t - t''$, $\xi_2 = t'' - t'$

$$\int dt' w(t')^4 w(t'-\tau)^4 \int d\xi_1\, d\xi_2 |K(\xi_1)|^2 |K(\xi_2)|^2 = \int dt' w(t')^4 w(t'-\tau)^4 \left(\int d\xi |K(\xi)|^2 \right)^2 \tag{C19}$$

Term 7:

$$\int dt\, dt'\, dt'' w(t)w(t-\tau)w(t')w(t'-\tau)w(t'')^2 w(t''-\tau)^2$$
$$\times K(t-t''+\tau)K(t'-t)K(t''-t'-\tau)K_0 \tag{C20}$$

Use new variables $\xi_1 = t - t'' + \tau$, $\xi_2 = t' - t$

$$K_0 \int dt'' w(t'')^2 w(t''-\tau)^4 w(t''-2\tau)^2 \int d\xi_1\, d\xi_2 K(\xi_1)K(\xi_2)K(-\xi_1-\xi_2) \tag{C21}$$

We now introduce a new number M_2

$$\frac{1}{M_2^2} = \frac{1}{K_0^3 T^2} \int d\xi_1\, d\xi_2 K(\xi_1)K(\xi_2)K(-\xi_1-\xi_2), \tag{C22}$$

and continue calculations for the specific model of the window function $w(t) = 1$ when $0 < t < T$ and zero outside. We have

$$\int dt\, w(t)^n w(t-\tau)^n = (T-\tau)h(T-\tau) \tag{C23}$$

and

$$\int dt\, w(t)^2 w(t-\tau)^4 w(t-2\tau)^2 = (T-2\tau)h(T-2\tau) \tag{C24}$$

Terms 2 and 7 add up to

$$\frac{2K_0^4 T^2}{M_2^2}(T-2\tau)h(T-2\tau) \tag{C25}$$

Terms 3 and 4 add up to

$$\frac{2K_0^4 T^2}{M_2^2}(T-\tau)h(T-\tau), \tag{C26}$$

and terms 6 gives

$$\frac{K_0^4 T^2}{M^2}(T-\tau)h(T-\tau). \tag{C27}$$

They combine into the following expression

$$\langle |A^{(f)}(\tau)|^2 A^{(p)}(\tau)\rangle = K_0^4 T^2 \left[\left(\frac{1}{M^2} + \frac{2}{M_2^2}\right)(T-\tau)h(T-\tau) + \frac{2}{M_2^2}(T-2\tau)h(T-2\tau)\right] \tag{C28}$$